Geomech. Geophys. Geo-energ. Geo-resour. (2024) 10:29
https://doi.org/10.1007/s40948-024-00753-1

RESEARCH

A fully coupled thermo-hydro-mechanical elastoplastic damage model for fractured rock

Nikolaos Reppas · Yilin Gui · Ben Wetenhall · Colin T. Davie · Jianjun Ma

Received: 24 October 2023 / Accepted: 13 January 2024

Abstract A detailed and fully coupled thermo-hydro-mechanical (THM) model for fractured rock is presented. This model distinguishes itself by harmoniously integrating elastoplastic material behaviour with a continuum damage mechanics framework. Solid matrix displacement, pore and fissure water pressures and temperature of the solid are introduced as the primary nodal variables. The ingenuity of this research is embedded in the intricate coupling of THM processes with plastic deformation and damage mechanics in a double porous medium, a venture that significantly broadens the remit of existing methodologies. The model is implemented using finite element method (FEM) and validation is achieved by comparing the FEM results against existing literature numerical outcomes describing linear and elastoplastic continuum damage behaviour of fractured rock. The model also exhibits an extraordinary proficiency in reproducing experimental triaxial test results, using THM components conjoined with elastoplastic bounding surface aspects and inherent hardening effects. It is imperative, nonetheless, to underscore the model's sensitivity to certain material properties, inclusive of strength parameters, leakage coefficients, and permeability attributes. This fully coupled THM model provides a comprehensive and sophisticated tool for investigating the behaviour of fractured rock under various loading conditions. It can help us better understand the physics of fractured rock behaviour and contribute to the development of more accurate and reliable models for engineering applications, such as CO_2 injection.

Article highlights

- Setup of fully coupled governing equations including: deformation, flow and energy balance.
- Construction of Thermo-Hydro-Mechanical (THM) constitutive model for fractured porous media.
- Implementation of bounding surface yield model considering elasto-plastic behaviour coupled with continuum damage effects and plastic hardening.

N. Reppas (✉) · B. Wetenhall · C. T. Davie
School of Engineering, Newcastle University, Newcastle Upon Tyne NE1 7RU, UK
e-mail: reppasnikolaos@gmail.com

Y. Gui (✉)
School of Civil and Environmental Engineering, Queensland University of Technology, Gardens Point, Brisbane, QLD 4000, Australia
e-mail: yilin.gui@qut.edu.au

Y. Gui
Centre for Materials Science, Queensland University of Technology, Gardens Point, Brisbane, QLD 4000, Australia

J. Ma
School of Civil Engineering, Sun Yat-Sen University, Guangzhou 510275, China

Published online: 25 January 2024

- Numerical implementation of the fully coupled THM model using FEM.

Keywords Rock · Fractured porous media · Coupled flow-deformation and heat transfer · Elastoplastic damage · FEM · Thermal loading · Constitutive modelling

1 Introduction

Coupling THM effects on fractured porous media is important to describe processes such as carbon storage, hydrogen storage, geothermal energy extraction, underground storage of thermal energy, gas-oil recovery, remediation of contaminated sites, isolation of hazardous waste, amongst others (Jing and Hudson 2002; Kolditz et al. 2016; Ma et al. 2016; Maedo et al. 2021; Bai and Tahmasebi 2022; Damirchi et al. 2022; Mahmoodpour et al. 2022; Saeedmonir and Khoei 2022; Aliyu et al. 2023). The first fully coupled flow-deformation analysis for elastic responses of saturated single porous media was considered in Biot (1941). Since then, the model has been widely adopted to describe pore pressure and effective stress distribution in saturated porous media (Detournay and Cheng 1988; Cheng et al. 1993). Throughout the literature, the most basic principles of THM modelling are demonstrated by Terzaghi's consolidation theory (von Terzaghi 1923), Biot's theory of elasticity (Biot 1941) and mixture theory (Goodman and Cowin 1972; Bowen 1982).

In recent years, more advanced models have been developed for deformable formations considering plasticity and continuum damage effects (Khalili and Loret 2001; Mortara 2009; Busetti et al. 2012; Shojaei et al. 2014; Ma 2016; Spiezia et al. 2016; Brünig and Michalski 2017; Zhao et al. 2018; Shen et al. 2019; Paluszny et al. 2020; Maedo et al. 2021; Ma et al. 2022; Kong et al. 2023; Zhang et al. 2023) including the coupling of elastoplastic damage models with micromechanics. These models adeptly capture phenomena such as strain softening and changes in elastic stiffness through the damage model, while accounting for irrecoverable strain and the residual state using plasticity theory. This coupling is crucial, as it enables the representation of permanent deformations within the material (Ma and Zhao 2018). However, despite these advancements, a critical gap exists in the consideration of coupled thermal effects within existing models. Current models, while adept at simulating mechanical and damage responses, often fall short of adequately addressing the thermal effects inherent in fractured rock formations.

Considering thermal loading in porous media, McTigue (1986) is one of the most cited research articles that considers local thermal equilibrium in rock and provides analytical results for the thermo-elastic behaviour of saturated porous rock with single porosity. The thermo-mechanical behaviour is based on Biot's (1941) poro-elasticity theory and on the isothermal theory of Rice and Cleary (1976). The characteristic of McTigue's model is that the thermal expansion of the porous medium is controlled by the solid skeleton only, the constitutive diffusion equations are based on Darcy's and Fourier's laws and a reduced form of the energy balance equation is presented as convective transport. Masters et al. (2000), assumed local thermal equilibrium among all phases and only one temperature variable was considered. Both convection and conduction are included in the model of Masters et al. (2000) and they validated their model with a double porosity isothermal problem and a non-isothermal single porosity example. For non-isothermal conditions, Bowen and Garcia (1970) introduced the thermo-mechanical theory of a mixture, in which each phase had its own temperature, considering non-linear elasticity, non-linear heat conduction, non-linear viscosity, and diffusion. Aifantis (1980) and Aifantis and Beskos (1980) were among the first to attempt non-isothermal models in fractured media, based on the assumption that the flow mechanism is convective in the fractures and conductive in the porous phase. De La Cruz and Spanos (1989) coupled the temperature variation and mechanical motion by considering separate temperature and heat transfer parameters for each phase of the saturated porous medium. Liu and Yu (2011), following the framework of Nishimura et al. (2009), recommended a coupled THM model to describe the behaviour of unsaturated porous media during freezing. Their model was based on thermodynamics and fluid mechanics. It took into consideration the elastoplastic deformation and the change of the volumetric heat capacity and ice content during freezing. Khalili and Selvadurai (2003), proposed a fully coupled THM model for fully saturated elastic double

porous media, assuming local thermal non-equilibrium. Thermal convection was accounted for between the phases, and three balance energy equations were proposed for the solid, porous and fracture domains (Khalili and Selvadurai 2003). Furthermore, the constitutive equations proposed by the THM model of Gelet et al. (2012) can be used to identify the possible failure of a borehole exposed to both temperature and pressure gradients. Tan et al. (2011) set up a coupled THM model describing the heat transfer and temperature distribution as well as water migration. They suggested a fully coupled THM model combined with a damage theory model, which could analyse the freeze–thaw stability of a tunnel under severe conditions. Huang et al. (2018) carried out a validation of the THM laboratory test conducted by Neaupane et al. (1999) by comparing it to a theoretical THM model, which was also numerically analysed, and found a good prediction of the heat and frost energy dissipation. Their validation demonstrated that all the critical parameters, including pore ice pressure, permeability, and thermal energy, were linked to the unfrozen water content. However, their test was limited to homogeneous and isotropic rock in which thermal transmission was the same in every direction during freezing. Finally, Ma et al. (2022) proposed a coupled THM elastoplastic damage model for concrete subjected to dynamic loading, focusing on thermal hardening due high temperature loading (20 °C < T < 950 °C) and triaxial conditions.

Previous investigations in the literature have generally not considered brittle–ductile behaviour, and existing damage models have demonstrated limitations in their capacity to explore phenomena such as fracturing, crack re-opening, or closure. Moreover, earlier models have struggled to simultaneously account for both thermal-hydro-mechanical (THM) effects and elastoplastic hardening influences. This study presents a groundbreaking constitutive model designed to emulate THM effects within a medium (rock) proximate to a wellbore. What sets this research apart is its integration of both thermal and elastoplastic continuum damage effects, departing from the conventional assumption of elasticity and isothermal conditions. This fully coupled THM double-porosity FEM model may be applied to simulate several wellbore stability scenarios during drilling and production of oil and gas; estimate any pore-fissure pressure and temperature evolution on a double porosity fractured medium during carbon sequestration due to different CO_2 injection scenarios; estimate the THM effects of thermal energy hydrogen storage, etc. This research expands the work of Ma et al. (2016) and Ma and Zhao (2018), introducing also thermal effects to rock, based on the work of Khalili and Selvadurai (2003), Gelet et al. (2012) and Ma et al. (2022). Hardening plasticity effects and permeability evolution are also considered in the proposed model based on the research of Khalili et al. (2008). The solution for the governing differential equations was obtained by numerical implementation of the constitutive model using an innovative finite element formulation developed in MATLAB.

2 Constitutive modelling

The model consists of a fully coupled THM formulation, where rock is treated as a two-phase system consisting of solid and liquid. The formulation presented consists of three separate inter-connected models considering deformation, flow, and heat exchange. Two interacting domains are identified: one representing the porous medium and the other the fracture network. Non-isothermal conditions are considered to exist in the double porous media during thermal loading, due to the different thermal diffusivity of the fluid in the pores and fissure and of the solid grains. However, adopting a non-isothermal model raises two issues: the correct termination of the work conjugate variables that describe the constitutive coupling laws and the definition of the heat transfer parameters between domains (Gelet et al. 2012). For the current research and for simplicity, the assumption that pores and fissures have the same temperature at each time step is adopted, i.e., the domains are in thermal equilibrium and one energy balance equation is written for the entire system. However, mass transfer between the domains is considered and the double porosity model of Khalili (2008) and Gelet et al. (2012) is adopted to describe the porous and fissure network.

The model is formulated as a coupled system of the partial differential governing equations, which are discretised in space by a finite element formulation and discretised in time by using the modified Euler's forward scheme with automatic sub-stepping. The set of coupled governing equations are non-linear, second-order differential equations that contain

both spatial and temporal derivatives of the primary variables, which are deformations, pore and fissure pressure and temperature of the solid. The solution of the discretised numerical model constructed from the differential equations can be used to solve the continuum problem as a linear problem using finite elements. The solutions produced by this technique for a typical boundary value problem are formed of both global and local solutions. For this research, the global solution scheme is used for the primary variables. The integrated constitutive model produces the local solutions, and variables such as stress, strain, plastic hardening, damage and permeability evolution are determined. In Fig. 1 the constitutive model flow chart can be seen. The detailed analytical formulation of the model and the constitutive relationships, as well as the damage evolution and hardening effects on rock are presented in the following sections.

2.1 Deformation model

The deformation model is described by the concept of geomechanical effective stress (Khalili and Valliappan 1996). According to Khalili and Selvadurai (2003), Gelet et al. (2012) and Bai (2016) and adopting Voigt's notation, the incremental form of the effective stress for saturated double porous media can be given as:

$$\dot{\boldsymbol{\sigma}}' = \dot{\boldsymbol{\sigma}} + j_1 \dot{p_1}\,\boldsymbol{\delta} + j_2 \dot{p_2}\,\boldsymbol{\delta} + \frac{C_{Ts}}{C_f}\dot{T}_s\boldsymbol{\delta} \tag{1}$$

where j_1 and j_2 are the effective stress parameters that relate, respectively, the pore pressure and fissure pressure to the matrix deformation vector; $\boldsymbol{\delta}$ is Kronecker's delta function; $\dot{\boldsymbol{\sigma}}$ is the incremental total stress; $\dot{p_1}$, $\dot{p_2}$ and $\dot{T}_s$ are the increments of pore and fissure fluid pressures and temperature of the solid respectively; and $\frac{C_{Ts}}{C_{fr}}$ is the ratio between the volumetric thermal expansion of the solid and the compressibility of the fracture domain. Based on Khalili et al. (2010), the volumetric thermal expansion coefficient of a whole porous medium is fully determined and equal to the thermal expansion of the solid skeleton. The effective stress parameters can be expressed as follows:

$$\begin{aligned} j_1 &= C_p / C_{fr} - C_s / C_{fr} \\ j_2 &= 1 - C_p / C_{fr} \end{aligned} \tag{2}$$

where C_p, C_{fr} and C_s represent the drained tangent elastic compressibilities of the porous medium, the fractured porous domain and the solid skeleton, respectively.

Selecting a representative volume of the fractured porous medium as an element, and assuming

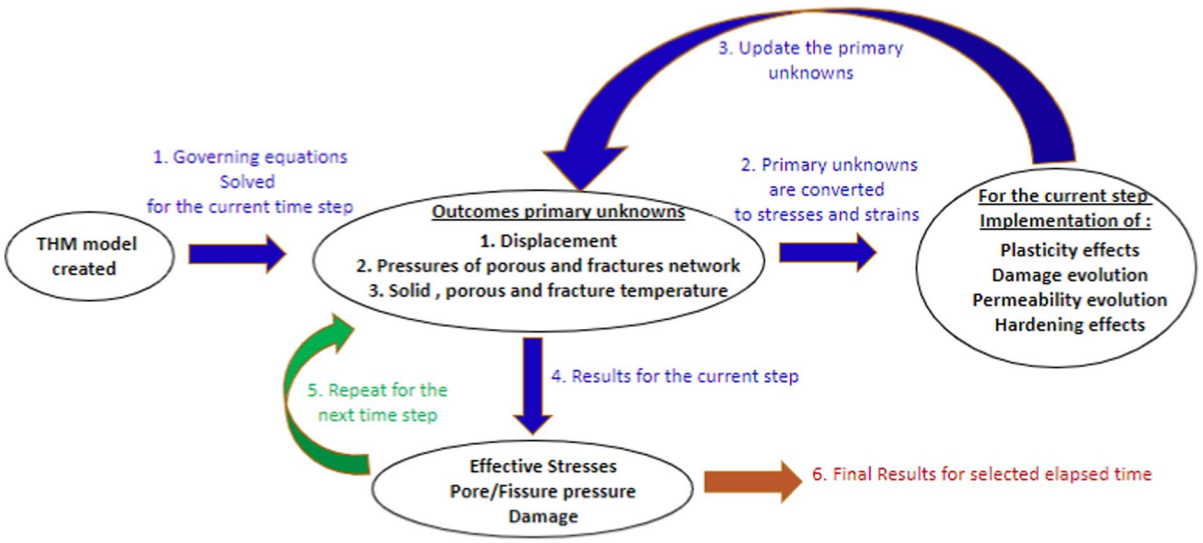

Fig. 1 Flowchart of constitutive model implementation

no internal acting forces, the linear momentum equation for the whole element can be expressed as:

$$div\boldsymbol{\sigma} + \boldsymbol{F} = 0 \tag{3}$$

where $\boldsymbol{\sigma}$ is the total external stress and $\boldsymbol{F}$ represents the body force per unit volume.

For the case of small deformations, the total strain component can be expressed as:

$$\boldsymbol{\varepsilon} = \frac{1}{2}(\nabla \boldsymbol{u} + \boldsymbol{u}\nabla) \tag{4}$$

where $\boldsymbol{u}$ is the displacement vector of the solid phase.

The incremental stress–strain relationship can be indicated as:

$$\dot{\boldsymbol{\sigma}}' = [\boldsymbol{C}]\dot{\boldsymbol{\varepsilon}} \tag{5}$$

where $\boldsymbol{C}$ is the tangential drained stiffness of the solid matrix of the damaged material including any elastic thermal effects and $\dot{\boldsymbol{\varepsilon}}$ is the strain increment of the solid skeleton.

Following Eqs. (1)–(5) the partial differential equation for the deformation model of a thermo-elastic double porous medium is described as follows:

$$div\left(\frac{1}{2}[\boldsymbol{C}](\nabla \dot{\boldsymbol{u}} + \dot{\boldsymbol{u}}\nabla) - j_1 \dot{p_1}\,\boldsymbol{\delta} - j_2 \dot{p_2}\,\boldsymbol{\delta} - \frac{C_{Ts}}{C_{fr}}\dot{T}_s\boldsymbol{\delta}\right) + \dot{\boldsymbol{F}} = 0 \tag{6}$$

C_{fr} according to Khalili et al. (2008) can be expressed in terms of Young's modulus (E) and Poisson's ratio (ν) as:

$$\begin{cases} C_{fr} = \frac{(1-2\nu)(1+\nu)}{(1-\nu)E}, & \textit{for 1D strain conditions} \\ C_{fr} = \frac{2(1-2\nu)(1+\nu)}{E}, & \textit{for 2D strain conditions} \\ C_{fr} = \frac{3(1-2\nu)}{E}, & \textit{for 3D strain conditions} \end{cases} \tag{7}$$

2.2 Flow model

The flow of fractured rock, in the pores and fissures, is determined by linking Darcy's law with the fluid and temperature gradient mass balance equation. Disregarding any internal and viscous effects, considering an isotropic porous material, Darcy's law is as follows:

$$\boldsymbol{v}_a^r = -\frac{\boldsymbol{k}_a}{\mu}\left(\nabla p_a + \rho_f \boldsymbol{g}\right) - \varphi_a \Theta \nabla T, a = 1, 2 \tag{8}$$

where $a = 1, 2$ represent the porous and fracture networks respectively, $\boldsymbol{v}_a^r$ is the relative velocity of the fluid, $\boldsymbol{k}_a$ is the average permeability, ∇p_a is the fluid pressure gradient, ρ_f is the density of the fluid, μ is the dynamic viscosity of the fluid, $\boldsymbol{g}$ is the vector of gravitational acceleration, φ_a is the porosity of pores or fissures, and Θ is the thermo-osmosis coefficient coupling fluid flux to the temperature gradient.

The relative velocity of the fluid can be expressed as:

$$\boldsymbol{v}_a^r = \varphi_a\left(\boldsymbol{v}_a - \boldsymbol{v}_s\right) \tag{9}$$

where $\boldsymbol{v}_a$ is the absolute fluid velocity and $\boldsymbol{v}_s$ is the velocity of the solid structure.

Ma et al. (2016) and Bai (2016) suggested that by considering the conservation of mass and the mass exchange between the porous medium and fissure network, the mass balance equation for a double porosity system can be given as:

$$-div\left(\varphi_a \rho_f \boldsymbol{v}_s\right) - div\left(\rho_f \boldsymbol{v}_a^r\right) = \frac{\partial}{\partial t}(\varphi_a \rho_f) + (-1)^a \gamma\left(p_1 - p_2\right) \tag{10}$$

where p_1, and p_2 are the pore and fissure fluid pressures, respectively, and γ is the shape factor for quasi-steady-state conditions that controls the exchange of fluid mass between the porous matrix and the fissure network and it is expressed according to Warren and Root (1963) as:

$$\gamma = \frac{4\omega(\omega+2)}{l^2} \tag{11}$$

where ω is the number of the total sets of fractures and l is the characteristic dimension for matrix blocks, which can be expressed from surface-volume ratio following the work of Bai (2016) as follows:

$$l = \begin{cases} \frac{3d_1d_2d_3}{(d_1d_2+d_2d_3+d_1d_3)}, & \omega = 3 \\ \frac{2d_1d_2}{(d_1+d_2)}, & \omega = 2 \\ d_1, & \omega = 1 \end{cases} \tag{12}$$

where d_1, d_2, and d_3 is the average fissure spacing along three orthogonal directions.

Applying the Lagrangian total derivative concept to Eq. (9) the flow equation will be as follows:

$$-\rho_f div\left(\boldsymbol{v}_a^r\right) = \varphi_a \frac{d_a\rho_f}{dt} + \rho_f \frac{d_s\varphi_a}{dt} + \varphi_a\rho_f div\left(\boldsymbol{v}_s\right) + (-1)^{a+1} \gamma\left(p_1 - p_2\right) \tag{13}$$

The term $\frac{d_a\rho_f}{dt}$ can be rewritten using the coefficient of fluid compressibility (C_{fl}) and the thermal expansion coefficient of the fluid (C_{Tf}) following Khalili et al. (2008) as:

$$\frac{d_a\rho_f}{dt} = C_{fl}\rho_f \frac{d_a p_a}{dt} - \rho_f C_{Tf} \frac{d_a T_a}{dt} \tag{14}$$

where T_a is the water temperature in the porous and fissure domain.

According to Ma et al. (2016), the divergence of the velocity of the solid structure can be expressed as follows:

$$div\left(\boldsymbol{v}_s\right) = \frac{1}{V_{total}} \frac{d_s V_{total}}{dt} \tag{15}$$

The term $\frac{d_s\varphi_a}{dt}$ from Eq. (13) can be also expressed as:

$$\frac{d_s\varphi_a}{dt} = \frac{1}{V_{total}} \left(\frac{d_s V_a}{dt} - \varphi_a \frac{d_s V_{total}}{dt} \right) \tag{16}$$

2.3 Heat transfer to the solid medium

The heat transfer is due to the temperature gradient only and can be described by the multi-dimensional extension of Fourier's Law as:

$$\boldsymbol{q}_s = -\varphi_s k_s \nabla T_s \tag{17}$$

where $\boldsymbol{q}_s$ is the conductive heat flux, φ_s is the porosity of the solid and k_s is the thermal conductivity of the solid.

According to Gelet et al. (2012) and Bai (2016) and assuming that the pore-fluid, fissure-fluid and solid are in local equilibrium, the energy balance equation for the solid phase can be presented as:

$$div\left(\varphi_s k_s \nabla T_s\right) = T_s \dot{s}_{solid} \tag{18}$$

where $\dot{s}_{solid}$ is the change in entropy per unit volume which can be expressed, following Bai (2016), as:

$$\dot{s}_{solid} = \frac{C_{Ts}}{C_f}\dot{\varepsilon} - \left(j_1 - \varphi_1\right) C_{Ts}\dot{p_1} - (j_2 - \varphi_2) C_{Ts}\dot{p_2} + \frac{\rho^s C_{ps}}{T_s}\dot{T}_s \tag{19}$$

where C_{ps} is the possible heat capacity of the solid (J/m^3 K) and ρ^s is the apparent density of the solid (kg/m^3), which is equal to the porosity of the solid $\left(\varphi_s\right)$ multiplied by the intrinsic density of the solid $\left(\rho_s\right)$.

2.4 Damage variable

For a certain Representative Elementary Volume (REV), big enough to contain several discrete microcracks; a plane normal to the direction vector ($\boldsymbol{n}_s$) is considered, which has an area (A) consisting of a damaged area (A_D) and an undamaged area (A_u). If we denote D as the damage variable linked to the vector ($\boldsymbol{n}_s$) then it is a scalar for isotropic damage and anisotropic operations:

$$D = \frac{A_D}{A} \tag{20}$$

In fracture mechanics, a fracture takes place when the current principal tensile stress exceeds the tensile strength in the stress domain. However, rock materials are exposed to both hydrostatic and deviatoric stress. Consequently, the equivalent stress or Von-Mises criterion is applied. Von-Mises criterion is applicable for the analysis of plastic deformation for ductile materials. The yielding of the ductile material begins when the second invariant of deviatoric stress J_2 reaches a critical value. The equivalent stress is equal to the deviatoric stress as $\sigma_e = \sqrt{3J_2}$.

The damage evolution law based on the Von-Mises criterion following the work of Yazdchi et al. (1996), Lemaitre (1985), Kachanov (1980) and Ma (2014) is:

$$\dot{D} = \begin{cases} \mathrm{H}_{\sigma_e}\left(\sigma_e\right)^{1/m}, & \sigma_e > \sigma_{et} \\ 0, & \sigma_e \le \sigma_{et} \end{cases} \tag{21}$$

where H_{σ_e} is the damage evolution rate and depends on the stress state (confining pressure and stress ratio):

$$\mathrm{H}_{\sigma_e} = h_{\sigma_e} |lnz| \left| ln\left(\frac{M_{cs} + \eta}{2M_{cs}} \right) \right| \tag{22}$$

where z controls the effects of the confining pressure on material behaviour and is expressed as

$z = p'_o \Big/ \left(p'_{conf} + 1\right)$, with the p'_o being the maximum hydrostatic compressive pressure or the historic consolidation pressure and p'_{conf} is the confining pressure; h_{σ_e} is a material constant that may be determined by fitting to experimental results; $\eta = \frac{q}{p'}$ can be used to determine the relationship between deviatoric and hydrostatic stresses (this is important as, generally, hydrostatic stress can be responsible for the closure of micro-cracks, and we need to discover the propagation of the micro-cracks); and M_{cs} is the slope of the critical state line. Based on these, the threshold of the damage equivalent stress σ_{et} can be expressed as (Ma et al. 2016):

$$\sigma_{et} = \sigma_{et0} + \frac{k_{\sigma_e} p' \exp(1/h)}{(1-D)} \tag{23}$$

where σ_{et0} is the initial threshold of damage equivalent stress, $k_{\sigma_e} > 0$ is a rock constant that controls the increase in the rate for the damage equivalent stress threshold. The hydrostatic stress p' is responsible for the development of micro-cracks and the plastic hardening or softening of the rock is determined by the plastic hardening energy h.

2.5 Constitutive relationships

According to the framework of continuum damage mechanics (Lemaitre 1985; Voyiadjis and Kattan 2005; Ma et al. 2016), the irrecoverable energy dissipation ψ consists of two parts: the damage elastic part ψ_e and the damage plastic part ψ_p. In this work, the plastic and elastic parts are denoted using the labels 'p' and 'e' respectively. In isothermal conditions, the irrecoverable energy dissipation ψ is expressed as:

$$\psi = \psi_e + \psi_p = \frac{1}{2}\left[\boldsymbol{\varepsilon}^e\right]^T \left[\boldsymbol{S_{DT}}\right]\left[\boldsymbol{\varepsilon}^e\right] + \psi_p \tag{24}$$

where $\boldsymbol{\varepsilon}^e$ is the second-order symmetric elastic strain tensor and $\boldsymbol{S_{DT}}$ is the fourth-order elastic stiffness tensor for the damaged material including elastic thermal effects. Thermal influence is included in the elastic strain using:

$$\boldsymbol{S_{DT}} = (1-D)^2 \boldsymbol{S_T} \tag{25}$$

where $\boldsymbol{S_T}$ is the fourth-order elastic stiffness of the undamaged material considering only thermal elastic deformations.

The effective stress, is presented as the derivative of the energy dissipation to the derivative of the elastic strain:

$$\boldsymbol{\sigma'} = \frac{\partial \psi}{\partial \boldsymbol{\varepsilon}^e} = \left[\boldsymbol{S_{DT}}\right]\left[\boldsymbol{\varepsilon}^e\right] \tag{26}$$

By differentiating Eq. (26), the stress rate (using Einstein convection) is determined as follows:

$$\dot{\boldsymbol{\sigma}}' = -\frac{2\dot{D}}{1-D}\left[\boldsymbol{S_{DT}}\right] : \boldsymbol{\varepsilon}^e + \left[\boldsymbol{S_{DT}}\right] : \dot{\boldsymbol{\varepsilon}}^e \tag{27}$$

Equation (27) can be rearranged to:

$$\dot{\boldsymbol{\sigma}}' = \left[\boldsymbol{S_{DT}}\right] : \dot{\boldsymbol{\varepsilon}}^d \tag{28}$$

in which

$$\dot{\boldsymbol{\varepsilon}}^d = \dot{\boldsymbol{\varepsilon}}^e - \frac{2\dot{D}}{1-D}\boldsymbol{\varepsilon}^e \tag{29}$$

According to Khalili and Valliappan (1996), the elastic constitutive equation for fully saturated fractured porous media can be achieved using the Maxwell-Betti reciprocal work theorem. Applying Betti's theorem and using Eqs. (1), (28) and (29), the elastic strain components $(\dot{\boldsymbol{\varepsilon}}^e, \frac{1}{V_{total}}\frac{d_s V_a}{dt})$ are related to the stress components $(\dot{\boldsymbol{\sigma}}, \dot{p}_a)$ as follows:

$$\begin{aligned}\dot{\boldsymbol{\varepsilon}}^e &= \dot{\boldsymbol{\varepsilon}}^d + \frac{2\dot{D}}{1-D}\boldsymbol{\varepsilon}^e + \dot{\boldsymbol{\varepsilon}}^T \\ &= \frac{1}{\left[\boldsymbol{S_{DT}}\right]}\left(\dot{\boldsymbol{\sigma}} - j_1 \dot{p_1}\,\boldsymbol{\delta} - j_2 \dot{p_2}\,\boldsymbol{\delta}\right) \\ &\quad + \frac{2\dot{D}}{1-D}\boldsymbol{\varepsilon}^e - \frac{C_{Ts}}{C_{fr}}\dot{T}_s\end{aligned} \tag{30}$$

It is assumed that temperature changes induce elastic strain, which leads to isotropic elastic expansion. The change in the pore and fissure volume, presented in Eq. (15), over the current volume of the porous domain with respect to the moving solid can be expressed as (Khalili et al. (2008)):

$$\frac{1}{V_{total}}\frac{d_s V_1}{dt} = \frac{\dot{V}_1}{V_{total}} = -j_1\left(\dot{\boldsymbol{\varepsilon}}_v^e - \dot{\boldsymbol{\varepsilon}}_T\right) + j_{11}^e \dot{p_1} - j_{12}^e\left(\dot{p_2} - \dot{p_1}\right) + \varphi_1 \frac{C_{Ts}}{C_{fr}}\dot{T}_s \tag{31}$$

$$\frac{1}{V_{total}}\frac{d_s V_2}{dt} = \frac{\dot{V}_2}{V_{total}} = -j_2\left(\dot{\boldsymbol{\varepsilon}}_v^e - \dot{\boldsymbol{\varepsilon}}_T\right) + j_{22}^e \dot{p_2} - j_{21}^e\left(\dot{p_1} - \dot{p_2}\right) + \varphi_2 \frac{C_{Ts}}{C_{fr}}\dot{T}_s \tag{32}$$

where j_{11}^e, j_{22}^e, j_{21}^e, j_{12}^e are the elastic coefficients relating to the porous volumetric deformations and changes of the porous fluid pressures. The elastic coefficients can be obtained using:

$$j_{11}^e = \varphi_1 C_{fr} + j_{12}^e \tag{33}$$

$$j_{22}^e = \varphi_2 C_{fr} + j_{21}^e \tag{34}$$

$$j_{12}^e = j_{21}^e = \left(j_1 j_2 - \frac{\varphi_1 \varphi_2}{\varphi_1 + \varphi_2}\right) C_{fr} \tag{35}$$

The total strain increment of the solid skeleton and the fluid volume change rate are made up of elastic and plastic parts:

$$\dot{\boldsymbol{\varepsilon}} = \dot{\boldsymbol{\varepsilon}}^e + \dot{\boldsymbol{\varepsilon}}^p \tag{36}$$

$$\frac{\dot{V}_a}{V_{total}} = \frac{\dot{V}_a^e}{V_{total}} + \frac{\dot{V}_a^p}{V_{total}} \tag{37}$$

Following the general plasticity approach and the definition of the effective stress concept, the incremental volumetric plastic strain rate and the incremental rates of fluid volumes in the porous and fracture domains can be expressed based on Ma et al. (2016) as follows:

$$\dot{\boldsymbol{\varepsilon}}^p = \dot{\lambda}\frac{\partial g}{\partial \boldsymbol{\sigma'}} \tag{38}$$

$$\frac{\dot{V}_1^p}{V_{total}} = \dot{\lambda}\frac{\partial g}{\partial p_a} = \dot{\lambda}\frac{\partial g}{\partial \boldsymbol{\sigma'}}\frac{\partial \boldsymbol{\sigma'}}{\partial p_a} = -j_1 \dot{\lambda}\boldsymbol{\delta}^T \frac{\partial g}{\partial \boldsymbol{\sigma'}} \tag{39}$$

$$\frac{\dot{V}_2^p}{V_{total}} = \dot{\lambda}\frac{\partial g}{\partial p_a} = \dot{\lambda}\frac{\partial g}{\partial \boldsymbol{\sigma'}}\frac{\partial \boldsymbol{\sigma'}}{\partial p_a} = -j_2 \dot{\lambda}\boldsymbol{\delta}^T \frac{\partial g}{\partial \boldsymbol{\sigma'}} \tag{40}$$

in which $\dot{\lambda}$ and $g(\boldsymbol{\sigma'})$ are the plastic multipliers and plastic potential as expressed by Khalili et al. (2008), respectively and presented in Appendix 1.

The yield function can be expressed in terms of effective stress and plastic hardening parameter as follows:

$$f\left(\boldsymbol{\sigma'}, p_c'(\dot{\boldsymbol{\varepsilon}}^p, D)\right) = 0 \tag{41}$$

where p_c' is a function of the plastic volumetric strain and damage that controls the size of the yield surface. The adopted bounding yield surface model can be found in the work of Khalili et al. (2005) and Ma (2014) and is presented in Appendix 1.

The consistency condition for the yield surface according to Ma and Zhao (2018) is presented as follows:

$$\dot{f} = \left(\frac{\partial f}{\partial \boldsymbol{\sigma'}}\right)^T \boldsymbol{\sigma'} + \frac{\partial f}{\partial p_c'}\left(\frac{\partial p_c'}{\partial \varepsilon_v^p}\dot{\boldsymbol{\varepsilon}}^p + \frac{\partial p_c'}{\partial D}\dot{D}\right) \tag{42}$$

According to Ma et al. (2016, 2022) and Reppas et al. (2022), the plastic hardening modulus h_p, which is presented analytically in Appendix 2, can be expressed as follows:

$$h_p = -\frac{\partial f}{\partial p_c'}\frac{\partial g}{\partial p'}\left(\frac{\partial p_c'}{\partial \varepsilon_v^p} + \frac{\partial p_c'}{\partial D}\frac{\dot{D}}{\dot{\varepsilon}_v^p}\right) \tag{43}$$

Then, substituting Eqs. (38) and (43) into Eq. (42), the consistency condition is rearranged as follows:

$$\dot{f} = \left(\frac{\partial f}{\partial \boldsymbol{\sigma'}}\right)^T \boldsymbol{\sigma'} - \dot{\lambda} h_p = 0 \tag{44}$$

where $\dot{\lambda}$ is the plastic multiplier for the damaged material and can be expressed as:

$$\dot{\lambda} = \frac{1}{H}\left(\frac{\partial f}{\partial \boldsymbol{\sigma'}}\right)^T \left[\boldsymbol{S_{DT}}\right]\left[\dot{\boldsymbol{\varepsilon}}^d\right] \tag{45}$$

The total hardening modulus $H = H(D)$ can be defined as:

$$H = h_p + \left(\frac{\partial f}{\partial \boldsymbol{\sigma'}}\right)^T [\boldsymbol{S_{DT}}] \left(\frac{\partial g}{\partial \boldsymbol{\sigma'}}\right) \tag{46}$$

The elastoplastic damage constitutive equation for the solid skeleton is outlined by substituting Eqs. (30)–(35) and (41) into (28) as follows:

$$\dot{\boldsymbol{\sigma}}' = [\boldsymbol{S_{DTp}}] : \dot{\boldsymbol{\varepsilon}}^d = \left([\boldsymbol{S_{DT}}] - \frac{1}{H}[\boldsymbol{S_{DT}}] \left(\frac{\partial f}{\partial \boldsymbol{\sigma'}}\right)^T \left(\frac{\partial g}{\partial \boldsymbol{\sigma'}}\right) [\boldsymbol{S_{DT}}]\right) : \dot{\boldsymbol{\varepsilon}}^d \tag{47}$$

Ma and Zhao (2018) suggested that the stiffness $\boldsymbol{S_{DTp}}$ of the double-porosity system is the drained elastoplastic fourth-order stiffness matrix of the damaged material. The elastoplastic stress-rate equation including temperature effects is presented as:

$$\dot{\boldsymbol{\sigma}} = [\boldsymbol{S_{DTp}}] : \dot{\boldsymbol{\varepsilon}}^d - \beta_1 \dot{p_1} \boldsymbol{\delta} - \beta_2 \dot{p_1} \boldsymbol{\delta} - \frac{C_{Ts}}{C_f} \dot{T}_s \boldsymbol{\delta} \tag{48}$$

Based on Eqs. (4) and (29), when damage occurs the damage strain rate is equal to:

$$\dot{\boldsymbol{\varepsilon}}^d = \frac{1}{2}\left(\nabla \dot{\boldsymbol{u}}_{\boldsymbol{d}} + \dot{\boldsymbol{u}}_{\boldsymbol{d}} \nabla\right) \tag{49}$$

2.6 Critical state concept

Critical state mechanics (CSM) has been extended to rock materials satisfactorily by many investigators (Gerogiannopoulos and Brown 1978; Shah 1997; Wong et al. 1997; Sheldon et al. 2006; Ma 2016; Reppas et al. 2020). While initially designed for soil analysis, these models have proven effective in capturing the intricate mechanisms of plastic strain exhibited by porous rocks (Cuss et al. 2003; Sheldon et al. 2006). Porous rocks, unlike low-porosity crystalline rocks, undergo deformation characterised by the localisation of zones prone to shearing, with the ability to shift around through processes such as shear, dilation, or compaction. This unique behavior arises from the rearrangement of their packing and the reduction in grain size of individual grains (Schultz and Siddharthan 2005). The versatility of CSM in accommodating such diverse rock behaviors is highlighted in the work by Navarro et al. (2010), where a model of this type successfully reproduces the main behaviour of rock using a relatively low number of parameters. This adaptability makes CSM a valuable tool for understanding and predicting the mechanical response of porous rocks under various conditions, contributing to advancements in geomechanics and rock engineering (Alonso et al. 2012).

The critical state is defined as the state at which the material approaches a large shear deformation at a constant shear stress (Khalili et al. 2008). The critical state line (CSL) separates the brittle and ductile deformation behaviour of rock. For critical state models, the damaged thermo-elastic modulus can be expressed as (Khalili et al. 2005; Reppas et al. 2022):

$$\boldsymbol{S_{DT}} = \begin{bmatrix} K_{DT} & 0 \\ 0 & 3G_{DT} \end{bmatrix} = \begin{bmatrix} (1-D)^2 \frac{vp'}{\kappa_T} & 0 \\ 0 & 3\frac{3(1-2\nu)}{2(1+\nu)} K_{DT} \end{bmatrix} \tag{50}$$

Where K_{DT} is the elastic bulk modulus considering thermal effects, G_{DT} is the elastic shear modulus considering thermal effects, $v = 1 + e$ is the specific volume, κ_T is the slope of the unloading- reloading line in a $v - lnp'$ domain, and ν is the Poisson's ratio of the material. Note, the thermal influence on κ_T is shown in Reppas et al. (2022).

2.7 Permeability evolution

Ma and Wang (2016) proposed a permeability evolution model for fissured porous sandstones under a wide range of confining pressures. The relationship between permeability and the overall porosity can provide an estimation of the permeability evolution:

$$k = k_0 \left(\frac{\varphi}{\varphi_0}\right)^{\Psi} \left(\frac{1}{\tau}\right)^{\varsigma} \tag{51}$$

where k, k_0 are the current and reference permeabilities, φ, φ_0 are the current and reference porosities, and Ψ and ς are the parameters of the permeability and permeability resistance.

The reference porosity $\varphi_0 = \frac{e}{1+e_0}$, according to Ma and Wang (2016), is obtained through physical

testing, and the current porosity can be calculated based on volumetric strain $\varepsilon_v = \varepsilon_1 + 2\varepsilon_3$ in a triaxial test, which can be found using the bounding surface of the presented model. According to Ma and Wang (2016), the fractured matrix solids are not deformable, and the volumetric change mainly comes from the change in pore space:

$$\varphi = \frac{e_0 - (1+e_0)\varepsilon_v}{1 + (e_0 - (1+e_0)\varepsilon_v)} \tag{52}$$

2.8 Summary of fully coupled equations

The fully coupled constitutive equations can be achieved by the combination of the deformation model, the flow model and the heat exchange. It is assumed that the temperature of the solid and the temperature of the liquid in the pores and fracture network is the same, for any specific point, at each time step.

The deformation equation after implementing Eqs. (47–49) into Eq. (6) is as follows:

$$div\left(\frac{1}{2}[\boldsymbol{S_{DTp}}](\nabla \dot{\boldsymbol{u}}_{\boldsymbol{d}} + \dot{\boldsymbol{u}}_{\boldsymbol{d}}\nabla) - j_1\dot{p_1}\boldsymbol{\delta} - j_2\dot{p_2}\boldsymbol{\delta} - \frac{C_{Ts}}{C_{fr}}\dot{T}_s\boldsymbol{\delta}\right) + \dot{\boldsymbol{F}} = 0 \tag{53}$$

The flow equations are expressed after implementing Eqs. (31–40) into Eq. (10):

$$div\left(\frac{\boldsymbol{k}_1}{\mu_f}(\nabla p_1 + \rho_f \boldsymbol{g}) + \varphi_1\Theta_1\nabla T\right) = \beta_1 div\dot{\boldsymbol{u}} + j_{11}\dot{p_1} - j_{12}\dot{p_2} - \varphi_1 C_T\dot{T}_1 - (j_1 - \varphi_1)C_{TS}\dot{T}_s + \gamma(p_1 - p_2) \tag{54}$$

$$div\left(\frac{\boldsymbol{k}_2}{\mu_f}(\nabla p_2 + \rho_f \boldsymbol{g}) + \varphi_2\Theta_2\nabla T\right) = j_2 div\dot{\boldsymbol{u}} + j_{22}\dot{p_2} - j_{21}\dot{p_1} - \varphi_2 C_T\dot{T}_2 - (\beta_2 - \varphi_2)C_s\dot{T}_s + \gamma(p_2 - p_1) \tag{55}$$

The energy balance equation for the solid medium is expressed after implementing Eqs. (19) and (30) into Eq. (18):

$$div(\varphi_s k_s \nabla T_s) = T_s\frac{C_s}{C_{fr}}div(\dot{u}) - T_s(\beta_1 - \varphi_1)C_s\dot{p_1} - T_s(\beta_2 - \varphi_2)C_s\dot{p_2} + \varphi_s C_{ps}\dot{T}_s - \omega_{s1}(T_1 - T_s) - \omega_{s2}(T_2 - T_s) \tag{56}$$

where the displacement vector can be expressed as $div\boldsymbol{u} = \boldsymbol{\delta}^T(\dot{\boldsymbol{\varepsilon}} - \dot{\boldsymbol{\varepsilon}}_T)$

The effective stress parameters are:

$$j_{12} = j_{21} = \left(j_1 j_2 - \varphi_1\varphi_2\frac{j_1 + j_2}{\varphi_1 + \varphi_2}\right)C_{fr} \tag{57}$$

$$j_{11} = \varphi_1 C_{fl} + (j_1 - \varphi_1)C_s + j_{12} \tag{58}$$

$$j_{22} = \varphi_2 C_{fl} + (j_2 - \varphi_2)C_s + j_{21} \tag{59}$$

3 Model validation

The fully coupled theoretical model presented in Eqs. (53–56) after converted into a FEM model (Appendix 3), is implemented in MATLAB and results from the literature are used to validate it. The selected geometry and mesh used for validation of the FEM model is presented in Fig. 2, based on the work of Kazemi (1969), Gelet et al (2012) and Ma and Zhao (2018). A unit thickness of the drawdown regime is used for the analysis. An axisymmetric plane stress formulation is adopted, as the loading conditions display symmetry about the vertical axis.

A vertical wellbore in a thermo-elastoplastic fractured medium is considered with inner radius $r_w = 0.1$ m, and an outer radius of 800 m at the far-field. A schematic illustration of the in-situ stresses and fluid pressure is presented in Fig. 2a, while the boundary

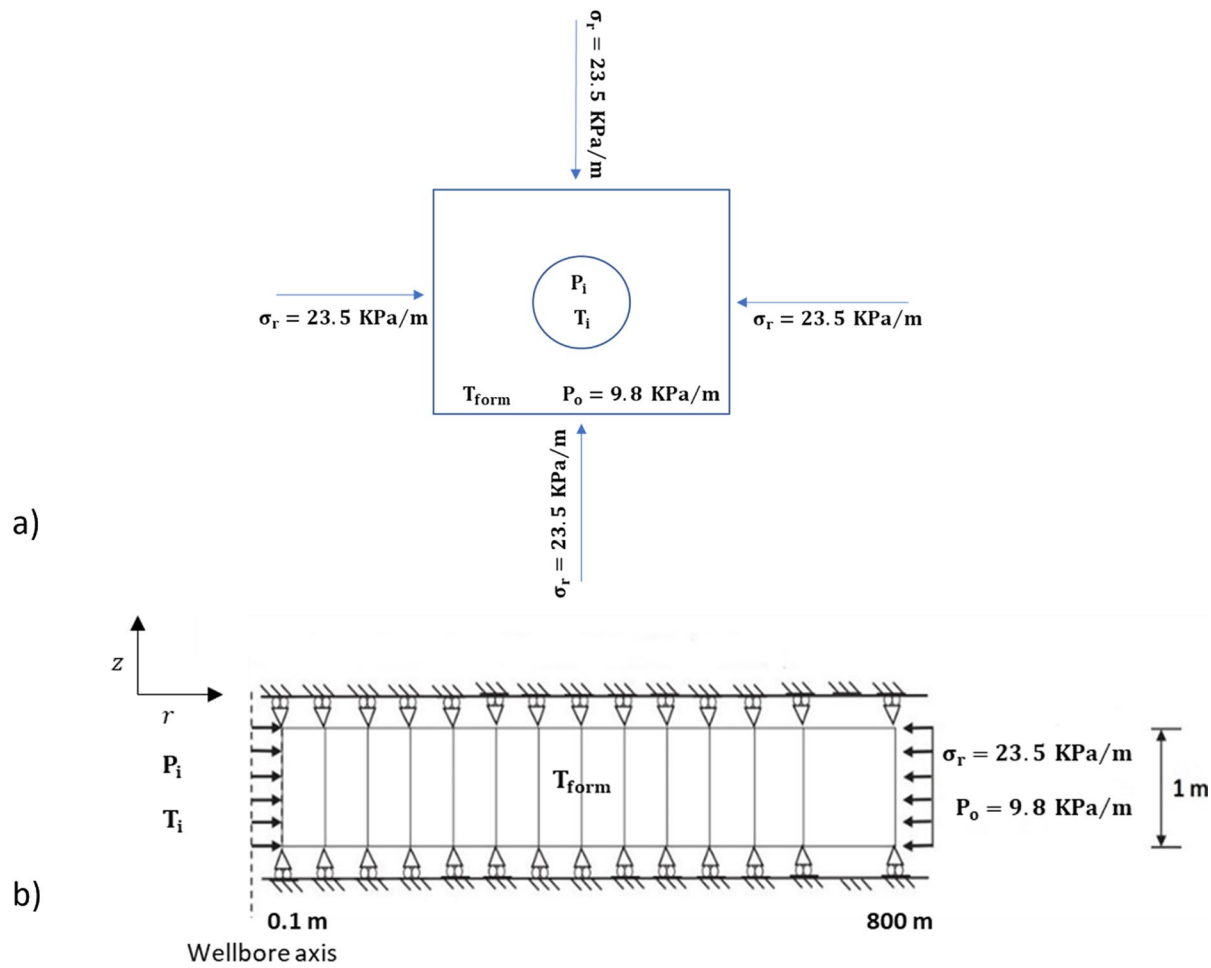

Fig. 2 **a** Schematic illustration of the well-plan view, **b** finite-element mesh and boundary conditions for axisymmetric problem (not to scale)

conditions are shown in Fig. 2b. P_o is the initial pore and fissure pressure before drilling and T_{form} is the temperature of the formation before applying any pressure or thermal loading. It is assumed that the three mediums have the same temperature for each time step, $T_1 = T_2 = T_s$. The fully saturated formation is located at a depth of 1000 m, and the subjected vertical gradients are presented in Fig. 2b. Distances of the horizontal grid points of the mesh (in m) from the centre of the wellbore are: [0.1, 0.101, 0.102, 0.105, 0.110, 0.115, 0.120, 0.125, 0.130, 0.140, 0.150, 0.20, 0.50, 1, 2, 5, 10, 20, 50, 100, 200, 500, 800].

Considering only elasticity and THM effects, the fully coupled FEM model is validated against the numerical results of Gelet et al (2012). Pore/Fissure pressures versus the radial distance from the wellbore wall are selected to validate two of the primary unknowns of the FEM model and effective stresses versus the radial distance from the wellbore wall are also compared to validate one of the secondary variables. For the damage evolution and plasticity effects, neglecting however any thermal loading, the model is validated against the work of Ma and Zhao (2018). Pore/Fissure pressures are compared to the work of Ma and Zhao (2018) to validate the influence of damage to the primary unknowns, while damage evolution validation makes the suggested damage-plasticity model robust.

Gelet et al. (2012) validated their model against a single porosity case (McTigue 1986). All the material moduli were set as inputs. The selected time for validation was t = 80 s. An internal pressure P_i and

Table 1 Material parameters for the elastic problem (Gelet et al. 2012)

Material parameters (symbol unit)	Value
Elastic modulus [E (GPa)]	9.5
Poisson's ratio [ν]	0.25
Storativity of the porous domain [β_{11} (MPa^{-1})]	7.23×10^{-09}
Storativity of the fissure network [β_{22} (MPa^{-1})]	1.8×10^{-10}
Effective stress parameter [β_1]	0.27
Effective stress parameter [β_2]	0.1
Compressibility of the fluid [c_f (MPa^{-1})]	1.45×10^{-9}
Fluid viscosity [μ (MPa)]	10^{-9}
Porosity of porous domain (φ_1)	0.15
Porosity of fissure network (φ_2)	0.015
Permeability of porous block [k_1 (m^2)]	5×10^{-20}
Permeability of fissure network[k_1 (m^2)]	5×10^{-19}
Fluid mass exchange parameter [γ (1/Pa s)]	5.3×10^{-10}
Heat capacity of the porous domain [C_{ps} (J/kg K)]	837
Thermal conductivity of the material [k_s (W/mK)]	2.65
Volumetric thermal expansion coefficient of the porous domain [C_{Ts} (1/K)]	1.8×10^{-5}
Volumetric thermal expansion coefficient of the fluid [C_{Tw} (1/K)]	4.5×10^{-4}

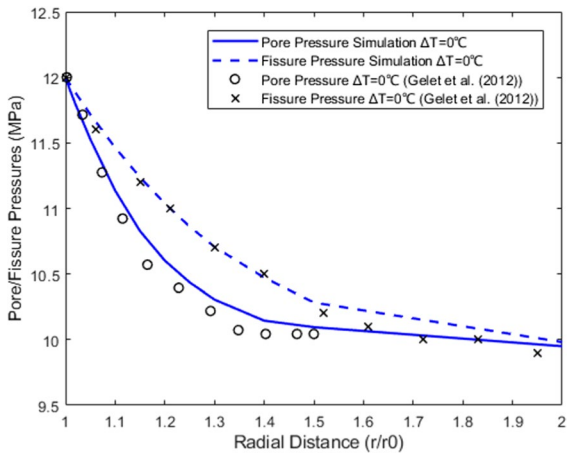

Fig. 3 Validation of pore and fissure pressure, at time 80 s for 0 °C temperature change (Gelet et al. 2012)

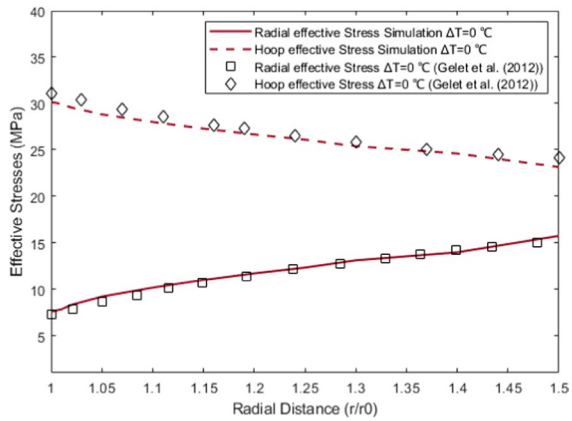

Fig. 4 Validation of the compressive Radial and Hoop effective stress, at time 80 s for 0 °C temperature change (Gelet et al. 2012)-absolute value presented

temperature T_i is applied representing the constant mud pressure of Gelet et al (2012). The internal selected pressure was $P_i = 12$ MPa. The internal temperature was set equal to $T_i = +50$ °C, 0 °C, −50 °C to validate the case scenarios of cooling or heating the fractured medium in the vicinity of the wellbore. The initial temperature of the formation was set to $T_{form} = 50$ °C. The material parameters used for the validation are presented in Table 1.

Figures 3, 4, 5, 6, 7 and 8 present the effect of temperature difference between the fluid in the wellbore and of the in-situ fluid at the wellbore wall. Figures 3, 5 and 7 present the effect of 0 °C, +50 °C, −50 °C thermal loading to the pore and fissure pressure of the wellbore wall, while Figs. 4, 6 and 8 examine the effect of the same thermal loading to the effective stresses of the wellbore. Based

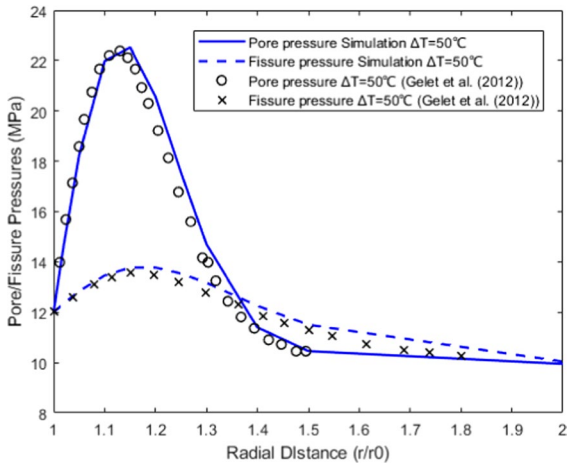

Fig. 5 Validation of pore and fissure pressure, at time 80 s for + 50 °C temperature change (Gelet et al. 2012)

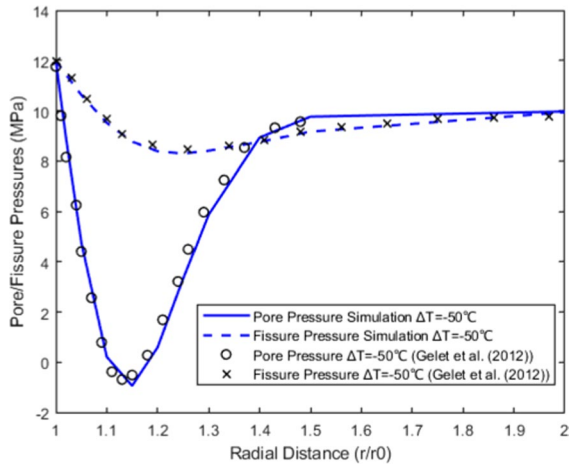

Fig. 7 Validation of pore and fissure pressure, at time 80 s for − 50 °C temperature change (Gelet et al. 2012)

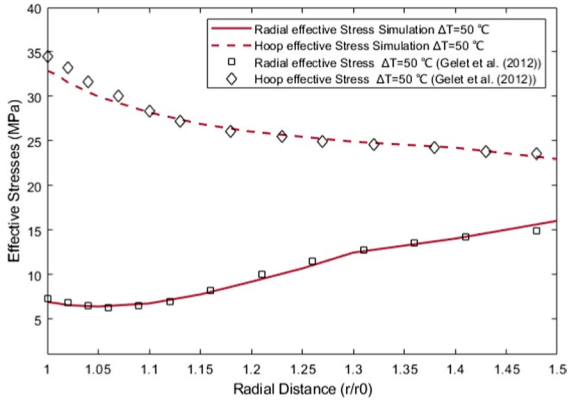

Fig. 6 Validation of the compressive Radial and Hoop effective stress, at time 80 s for + 50 °C temperature change (Gelet et al. 2012)-absolute value presented

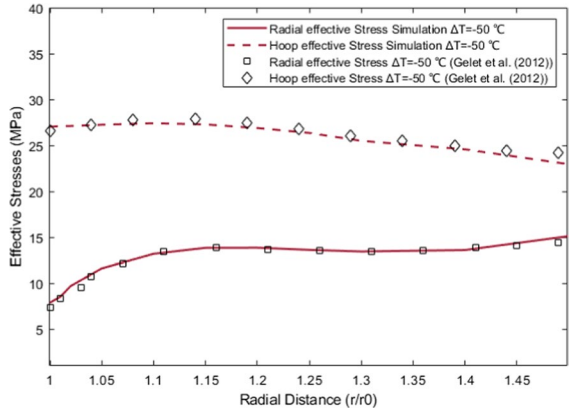

Fig. 8 Validation of the compressive Radial and Hoop effective stress, at 80 s for − 50 °C temperature change (Gelet et al. 2012)-absolute value presented

on the research of Gelet et al. (2012), the value of the radial stress at the well bore is not influenced by changing the temperature, while the hoop stress changes significantly. For this reason and adopting this assumption, the thermal expansion influence due to cooling or heating was applied only to the hoop stress as a boundary condition. The model agrees with the results of Gelet et al. (2012) and reasonably captures the behaviour of the rock in the vicinity of the wellbore, once temperature loading is applied. Additionally, the model seems to remarkably agree with both the pore/fissure pressures and the effective stresses.

According to Ma and Zhao (2018), elastic analysis gives an underestimation of the effective stresses and an overestimation of the fluid pressures. During loading, new created fractures or micro-cracks, which indicates damage, increase the porosity and reduce pore pressures (Detournay and Cheng 1988). Consequently, an elastoplastic model is appropriate for a more realistic scenarios. The damage evolution law was presented in Sect. 2.4 and is validated against the work of Ma and Zhao (2018), in which thermal effects are ignored and critical state mechanics are considered. The wellbore's internal pressure was

Table 2 Material parameters for the damage validation (Ma and Zhao 2018)

Material parameters (unit)	Value
Elastic modulus [E (GPa)]	10, 20, 100
Poisson's ratio [ν]	0.25
Storativity of the porous domain [β_{11} (MPa^{-1})]	7.23×10^{-09}
Storativity of fissure network [β_{22} (MPa^{-1})]	1.8×10^{-10}
Matrix coupling factor [$\beta_{12}=\beta_{21}$ (MPa^{-1})]	0
Effective stress parameter [β_1]	0.99
Effective stress parameter [β_2]	0.01
Compressibility of the fluid [c_f (MPa^{-1})]	1.45×10^{-9}
Fluid viscosity [μ (MPa^1)]	10^{-9}
Porosity of porous domain (φ_1)	0.04985
Porosity of fissure network (φ_2)	0.001243
Permeability of porous block [k_1 (m^2)]	5×10^{-20}
Permeability of fissure network [k_2 (m^2)]	5×10^{-19}
Fluid mass exchange parameter [γ (1/Pa s)]	5.3×10^{-10}
Gradient of isotropic compression line (ICL) [λ]	0.1
Slope of the unloading- reloading line (URL) [κ]	0.031
Parameter controlling the shape of the bounding surface [M]	1.9
Material constant of the bounding surface [R]	2.45
Slope of the Critical State Line (CSL) [M_{cs}]	1.7
Hardening material constant [k_d]	1

Table 3 Damage material parameters

k_m	Y_{D0}	m_D	m	h_γ
0.45	0.001	0.0025	10	0.00015

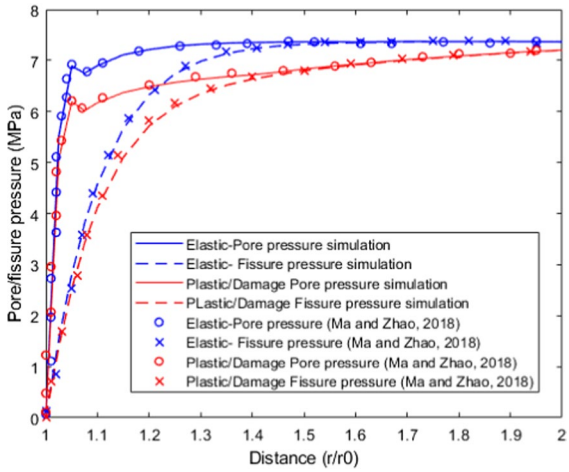

Fig. 9 Pore-Fissure pressure diagram with and without damage for a drilled borehole, validation for a material with E = 10 GPa

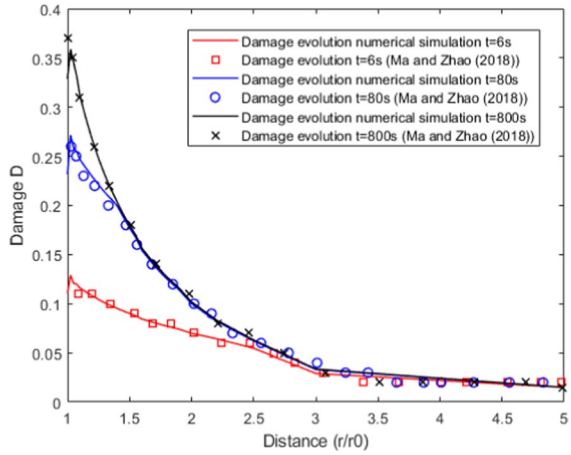

Fig. 10 Validation of damage evolution in different time steps for E = 10 GPa (Ma and Zhao 2018)

set as 0, indicating a post-drilling scenario. Based on Ma (2014) and Kazemi (1969), the initial stress state for material with elastic modulus $E = 10$ GPa is $p'_c = 35.3$ MPa and $\breve{p}'_c = 63$ MPa. The material properties and critical state mechanics parameters based on Ma and Zhao (2018) are listed in Table 2.

The damage variables used based on the work of Ma and Zhao (2018) are listed in Table 3:

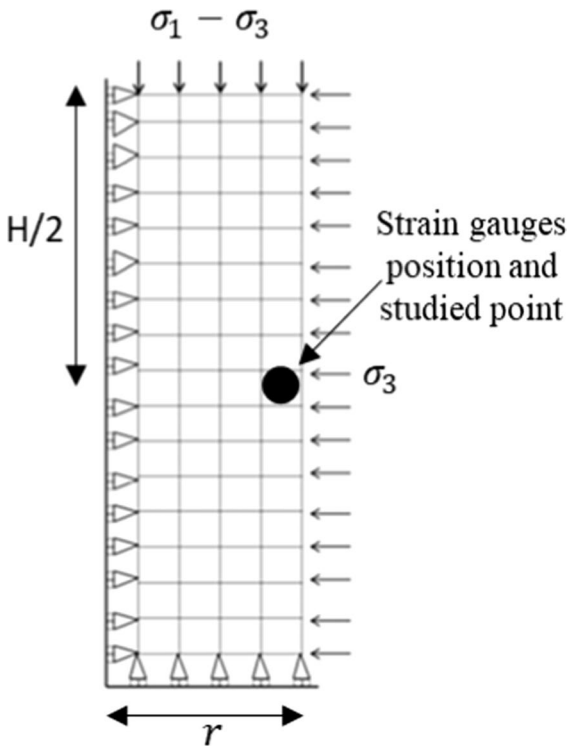

Fig. 11 The finite element mesh and boundary condition for the UCS and triaxial test simulation

The effective stress parameters were set equal to $j_1 = 0.99$ and $j_2 = 0.01$, based on Johnson and Cleary (1991), to reproduce the results of Ma and Zhao (2018). In Fig. 9 the fluid pressure response in the double porous fractured domain is presented considering both elastic and elastoplastic damage behaviour. The outcomes of the proposed model are compared to the numerical results of Ma and Zhao (2018), and satisfactoraly reproduce the effect of damage to the pore/fissure pressure at the vicinity of the wellbore for a particular time step (t = 80 s). In Fig. 10, the evolution of damage in time is also reproduced versus the radial distance from the wellbore, and the results fit satisfactoraly the outcome of Ma and Zhao (2018).

To validate the plasticity and hardening effects (Appendix 1), an axially symmetric mesh which consisted of 64 four-node quadrilateral elements with 2 by 2 integration points was considered. One-half of the sample was analysed, and the boundary conditions are presented in Fig. 11. The numerical model is used to reproduce experimental triaxial tests and validated against the experimental results of Reppas et al. (2023).

Based on Ma (2014), for strain increments smaller than 10^{-4}, the numbers of steps are sufficient to give a representative solution. Consequently, to reduce the computational time, the axial strain rate was set as 10^{-4}. The hardening parameters m_p, the material constant k_d, the slope of the unloading–reloading line κ, the critical state line's slope M_{cs} and the Poisson's ratio ν are taken from the research of Reppas et al. (2022) and Reppas et al. (2023) and presented in Table 4. The void ratio was estimated based on the experimental tests of Reppas et al. (2023) as $e_0 = 0.38$. Damage evolution

Table 4 Parameter values for 12.5 MPa (Reppas et al. 2022, 2023)

	ν	λ	κ	M_{cs}	m_p	k_d
15 °C	0.26	0.1	0.00125	1.55	5	37
− 5 °C	0.15	0.1	0.00299	1.66	12	37

Table 5 Rock samples dimensions and temperatures (Reppas et al. 2023)

Temperature	Samples	Diameter (mm)	Length (mm)	Dry mass (g)
Triaxial tests 12.5 MPa saturated sandstones				
15 °C	1	37.65	82.45	208.11
	2	37.60	83.14	199.18
	3	37.40	80.76	191.13
− 5 °C	4	37.79	79.31	201.60
	5	37.81	83.06	209.27
	6	37.91	81.74	203.68

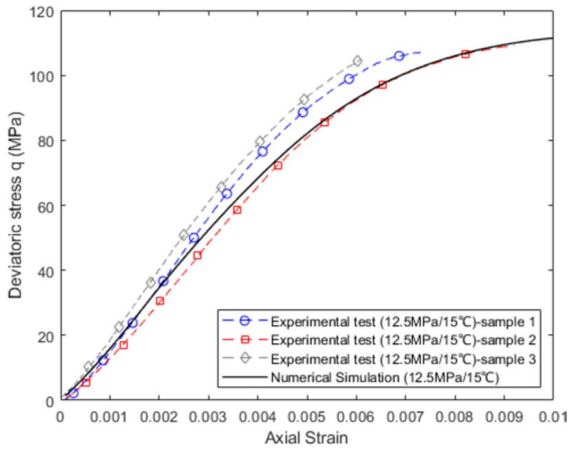

Fig. 12 Deviatoric stress-axial strain relationship for triaxial 12.5 MPa test at 15 °C. (Experimental tests and Numerical simulation)

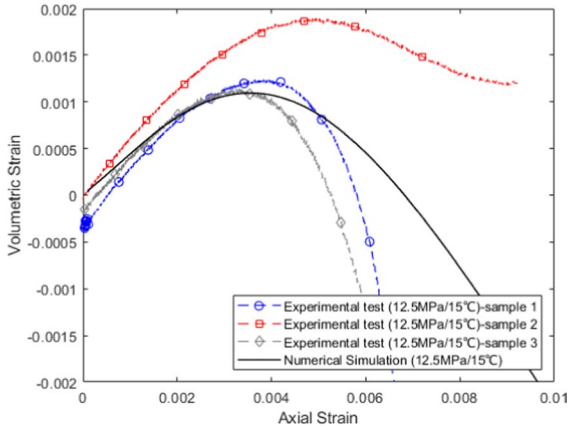

Fig. 13 Volumetric strain-axial strain relationship for triaxial 12.5 MPa test at 15 °C. (Experimental tests and Numerical simulation)

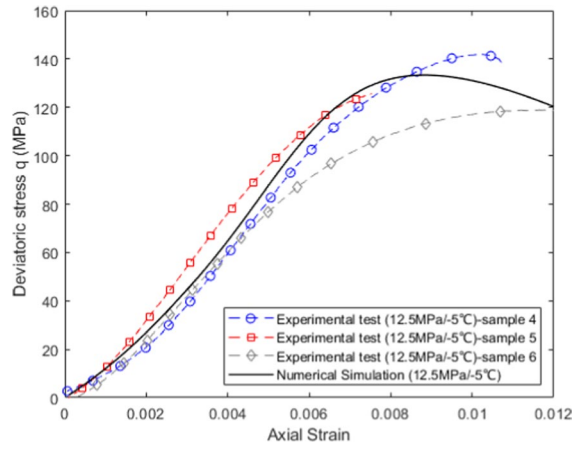

Fig. 14 Deviatoric stress-axial strain relationship for triaxial 12.5 MPa test at −5 °C. (Experimental tests and Numerical simulation)

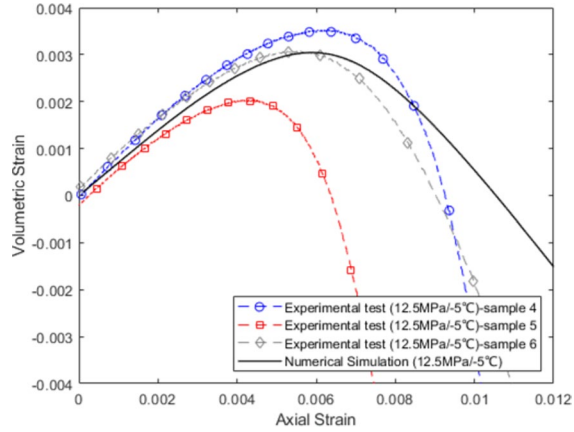

Fig. 15 Volumetric strain-axial strain relationship for triaxial 12.5 MPa test at −5 °C. (Experimental tests and Numerical simulation)

parameters and initial damage are assumed to be constant in all the tests with $D_{initial} = 0.015$. The damage parameters are the same as presented in Table 3. The numerical simulation is compared to a set of three triaxial tests with sample characteristics presented in Table 5.

It can be seen from Figs. 4, 5, 6, 7, 8 and 9 that the model reproduces the literature results, with a slight difference at the wellbore wall. Specifically, at the wellbore wall, hoop effective stresses are around 8% underestimated for positive thermal loading compared to the work of Gelet et al. (2012), while maximum damage in time is 4% lower than in the work of Ma and Zhao (2018). At a small radial distance from the wellbore wall and further to the far field the model is in perfect agreement with the literature results.

A robust representation of the experimental results (Figs. 12, 13, 14 and 15) can be seen for the deviatoric stress- axial strain curve while for the volumetric

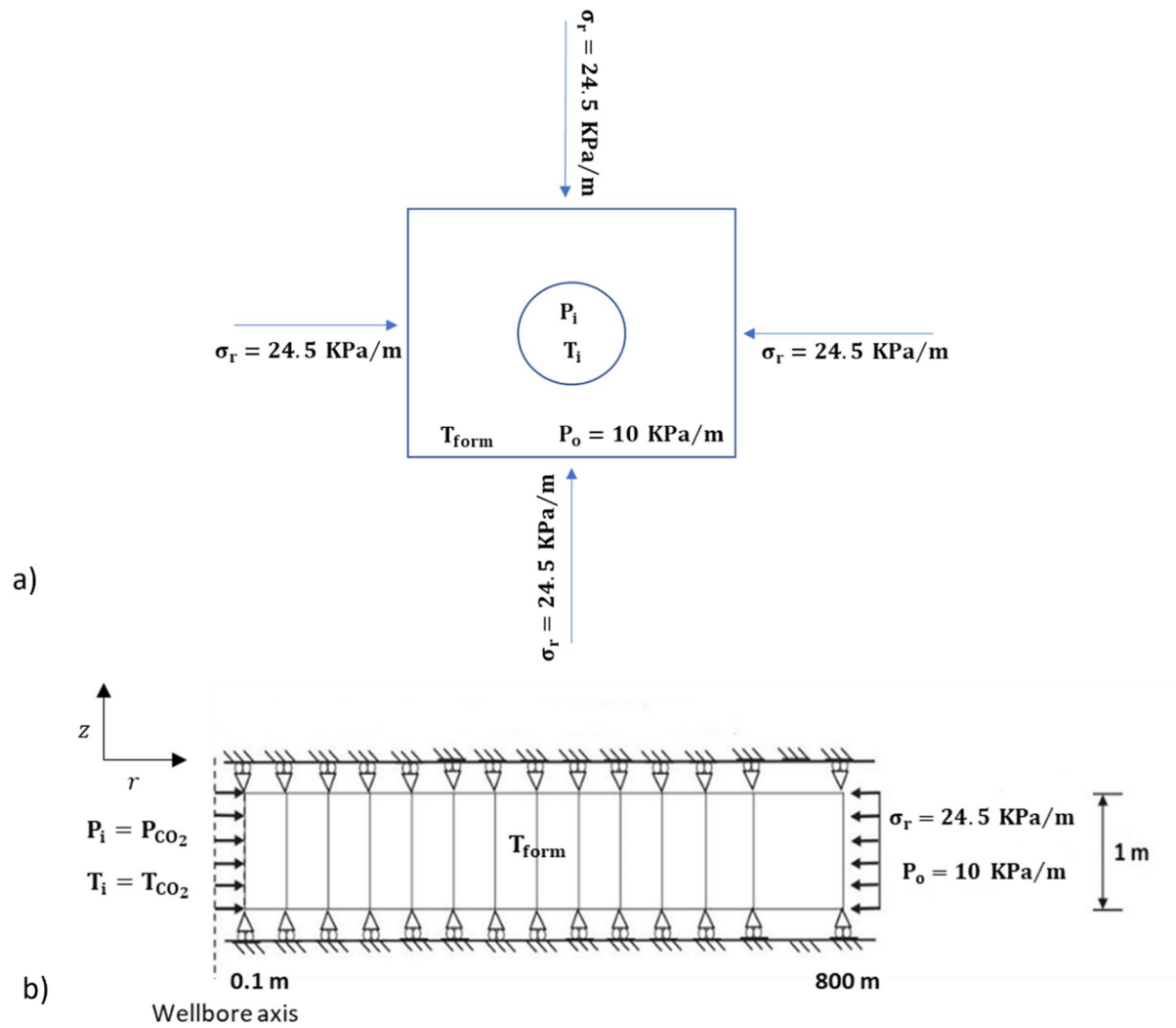

Fig. 16 **a** Schematic illustration of the injection well-plan view, **b** finite-element mesh and boundary conditions for axisymmetric problem (not to scale)

strain-axial strain curve there is good agreement until reaching nearly the 6% axial strain. This is mainly happening as the Poisson's ratio is increasing and the model cannot accept values of Poisson's ratio bigger than 0.5.

It can be said that by validating against an elastic THM model and against an elastoplastic hydro-mechanical model, as well as against experimental triaxial tests, the model seems robust and can be used to investigate different loading scenarios and examine various fluid-thermal-deformation examples.

4 Wellbore stability representative scenario and parametric study

4.1 Simulation of representative injection scenario

To demonstrate the capability of the model to simulate wellbore stability scenarios, the effects of internal wellbore pressures and temperatures, due to CO_2 injection or other applications, on the pore-fissure pressures, effective stresses and damage evolution of the surrounding rock are presented. A unit thickness

of the drawdown regime is analysed in this chapter. A vertical wellbore of inner radius $r_w = 0.1$ m is considered and a unit thickness of the wellbore is simulated, with the outer radius being set to 800 m to describe the boundary conditions at the far-field. Vertical deformation of the whole medium is assumed to be

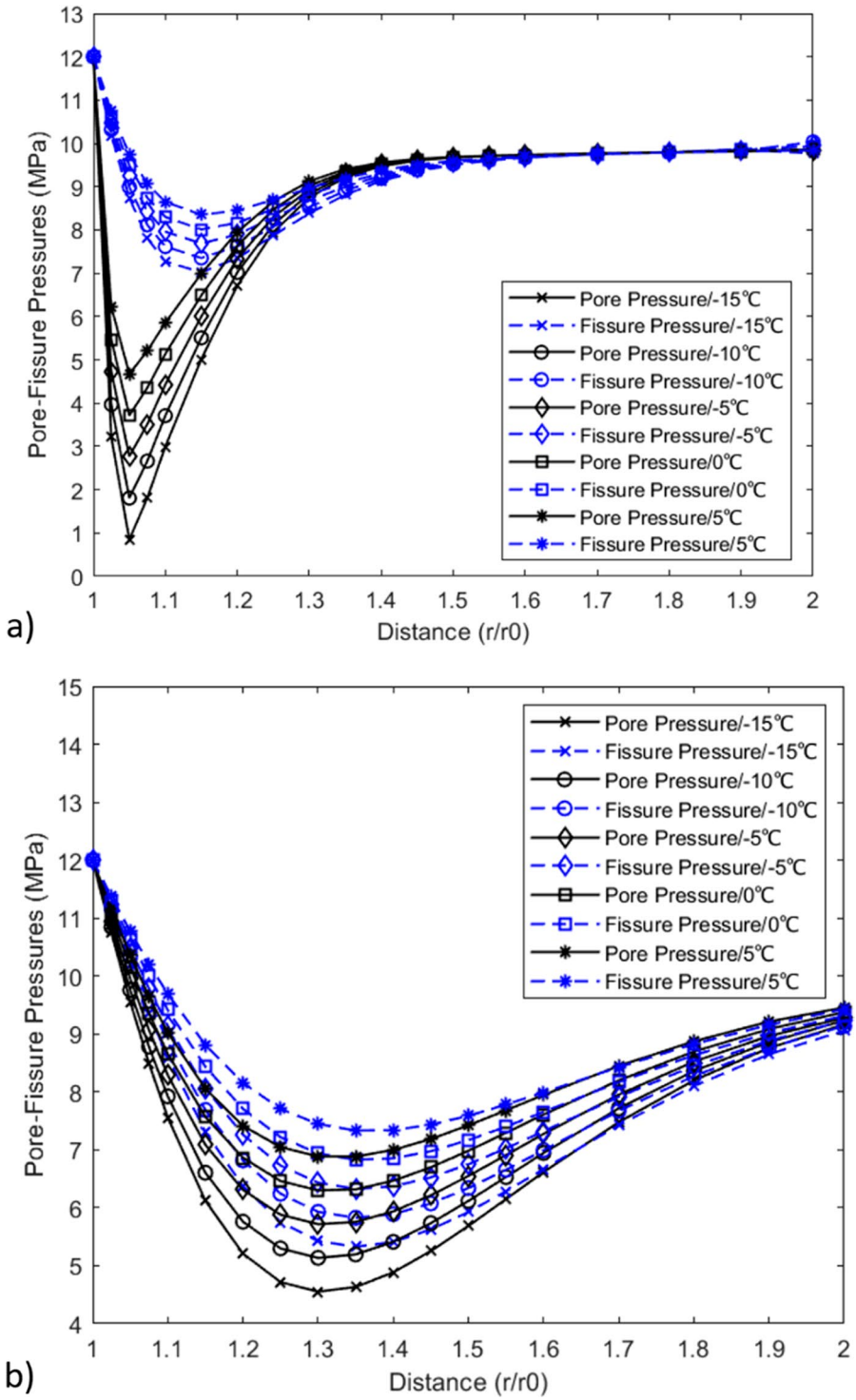

Fig. 17 Pore-Fissure pressure profiles in a dual-porosity system at **a** t = 80 s, **b** t = 800 s

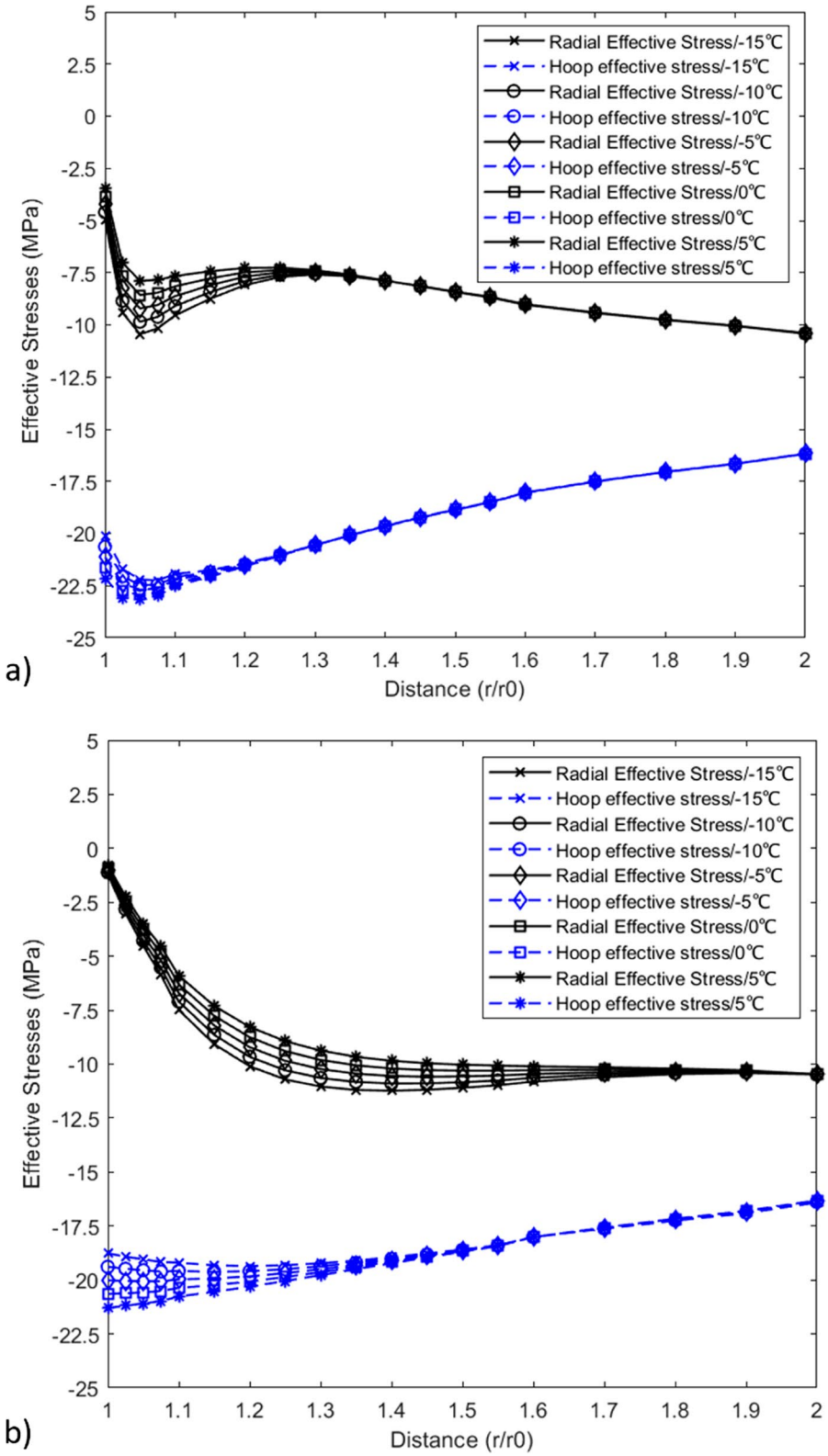

Fig. 18 Radial and Hoop effective stresses profiles in a dual-porosity system at **a** t = 80 s, **b** t = 800 s

constrained. Elastoplastic damage effects on the wellbore wall are considered and the isotropic material parameters for the parametric study were taken from Tables 1 and 2. The finite element mesh and boundary conditions of the problem can be seen in Fig. 16. Since the loading displays symmetry about the vertical axis of the wellbore, an axisymmetric formulation is selected. Coordinates, measured in meters from the centre of the wellbore, of the horizontal grid points of the mesh are: [0.1, 0.1025, 0.105, 0.1075, 0.110, 0.115, 0.120, 0.125, 0.130, 0.135, 0.140, 0.145, 0.150, 0.155, 0.160, 0.17, 0.180, 0.190, 0.20, 0.22, 0.25, 0.30, 0.50, 1, 2, 5, 10, 20, 50, 100, 200, 400, 600, 800]. This demonstrates that more points are considered close to the wellbore, which is the area of interest, as mesh refinement technique. The results are presented at time $t = 80$ s, and $t = 800$ s. The time ($t = 80$ s), corresponds to an early time response of the system, where the difference between the three temperatures is the largest.

Different scenarios are simulated to examine the behaviour of the rock during the injection of CO_2. The pressure of the CO_2 is considered as the internal pressure of the wellbore (P_i or P_{CO_2}) and the stress due to the weight of the formation as external radial stress (σ_r). The initial pore and fissure pressure, assuming the system to be in equilibrium, before injection, is equal to the hydrostatic pressure (P_0) and is influenced by effective stress parameters due to post drilling effects. The temperature of the formation (T_{form}) was selected according to the studied depth. It should be noted that the (P_0) and (T_{form}) are the pressure and temperature of the formation prior to any drilling. The internal temperature of the wellbore (T_i) was selected according to the injected temperature of the CO_2.

During CO_2 injection, typically the pressure and temperature of the CO_2 will increase with depth of the wellbore (Vilarrasa et al. 2013). An example of 1000 m depth, with $P_i = 24.5$ MPa and $T_{form} = 33$ °C, was selected based on Vilarrasa et al. (2013). The damage parameters for the damage evolution law which are based on the tensile principal stress are the same as those used in Table 3.

The simulated internal temperatures of the wellbore were − 15 °C, − 10 °C, − 5 °C, 0 °C, 5 °C. These temperatures were selected to identify the cooling effects on rock due to CO_2 injection. The range of them were based on the research of Vilarrasa et al. (2013). The pore-fissure pressures and the effective stresses results of simulations are presented in Figs. 17 and 18, respectively.

For internal wellbore temperature of − 15 °C, there is a huge drop of the pore pressure at the early stage of the simulation (t = 80 s), from 12 MPa to almost 1 MPa compared to the temperature of 5 °C (Fig. 16a). This can induce stress-relief and lead to rock fracturing (Khaledi et al. 2021). However, this pore pressure drop decreases as time passes and the pore and fissure pressure are trying to reach equilibrium. Additionally, for t = 80 s, the compressive radial stress increases for higher temperature difference while the hoop stress decreases. For 800 s, this change in effective stresses becomes more apparent.

Studying different material parameters is also important, as mechanical parameters can influence the induced damage of the material. Additionally, different temperature conditions can also alter the effective pressures of the rock. Young's modulus, leakage term and permeability evolution are investigated. Young's modulus describes the elastic behaviour of the material, leakage term controls the flow between the porous and fissure domain and permeability indicates how quickly the saline water flows inside the fractured porous domain. All of them can influence the outcome of the deformation, flow, and heat transfer.

4.2 Young's modulus E influence on the results

To identify the influence to the numerical simulation of E, two different injection temperatures are used: 5 °C and 33 °C. The temperature of the formation is considered $T_{form} = 33$ °C. These temperatures are selected to investigate if Young's modulus influence exist when there is a temperature difference between wellbore wall and formation.

In Figs. 19 and 20 the influence of Young's modulus on effective stresses and damage evolution is presented, respectively.

4.3 Leakage term influence on the results

The leakage parameter or aperture factor controls the transfer of mass between the porous block and the fissure domain in local thermal non-equilibrium. Values of the leakage term can vary from 5.3×10^{-11}/Pa s to 10^{-7}/Pa s (Kazemi 1969; Gelet et al. 2012). Three

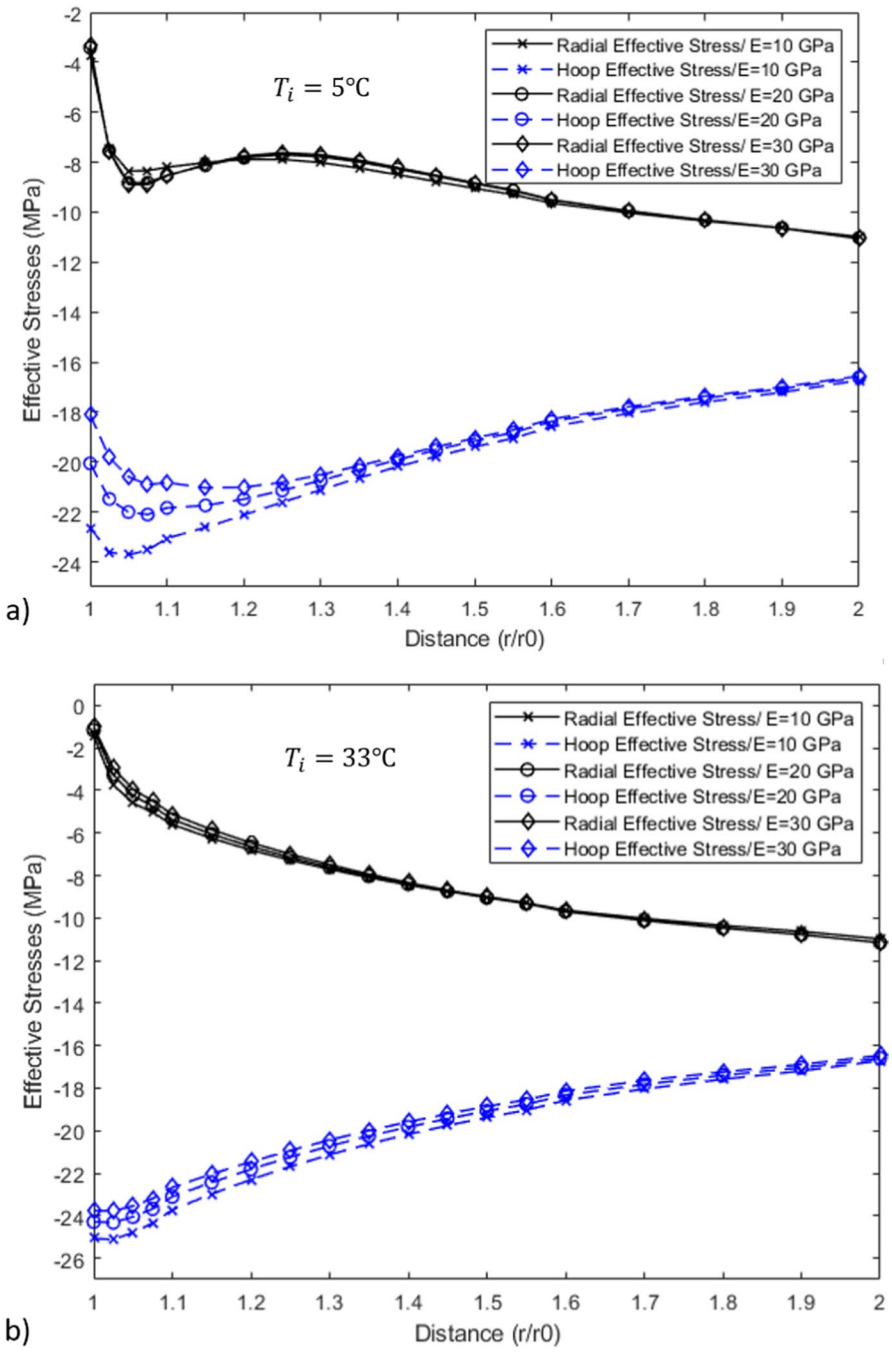

Fig. 19 Influence of Young's modulus (E) on the effective stresses of the rock under different internal temperatures **a** $T_i = 5$ °C and **b** $T_i = 33$ °C, t = 80 s

different values were used (10^{-7}, 10^{-9}, 10^{-11}) to study the influence of the fluid leakage parameter on the results. The temperature of the formation is considered $T_{form} = 33$ °C. The internal temperature for this parametric study is 5 °C corresponding to an injected temperature of −5 °C according to Vilarrasa and Laloui (2016). The same mesh, boundary conditions were used as described in Fig. 15. Young's modulus was set equal to 10 GPa, to focus the parametric study to the leakage aperture factor. In Fig. 21, the influence of the leakage term to the effective stresses of the wellbore is presented, while in Figs. 22 and 23 the effect of the leakage term to the pore-fissure rock pressures and damage is investigated, respectively.

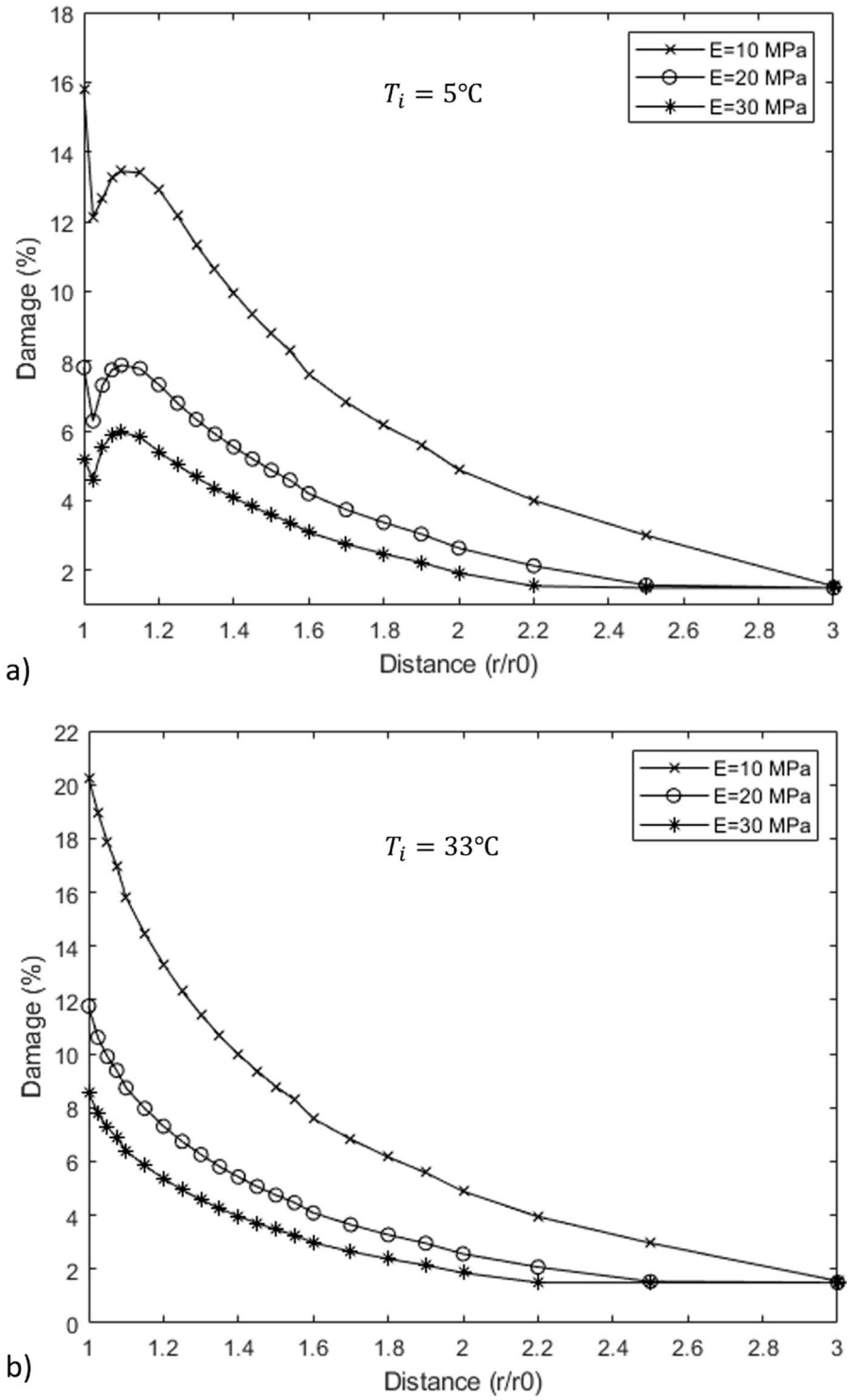

Fig. 20 Influence of (E) on the damage of the rock under different internal temperatures **a** $T_i = 5$ °C and **b** $T_i = 33$ °C, t = 80 s

From Fig. 21, the radial effective stress becomes more compressive as the aperture factor decreases, while the hoop effective stress is slightly changing. Additionally, it can be seen from Fig. 22 that lower leakage parameter induces higher pore pressure drop and increases the difference in pressure between the

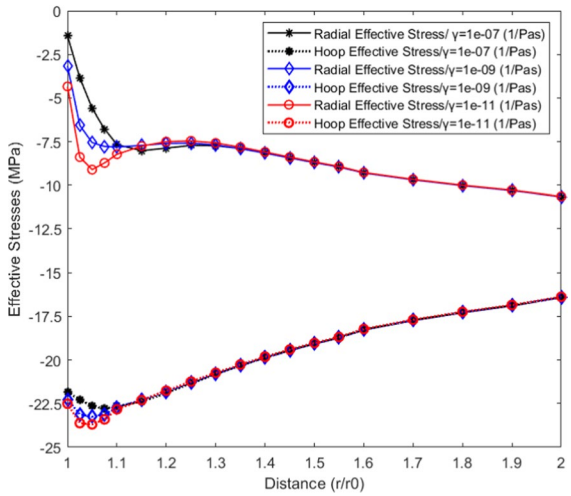

Fig. 21 Leakage term influence on effective stress ($T_i = 5$ °C)

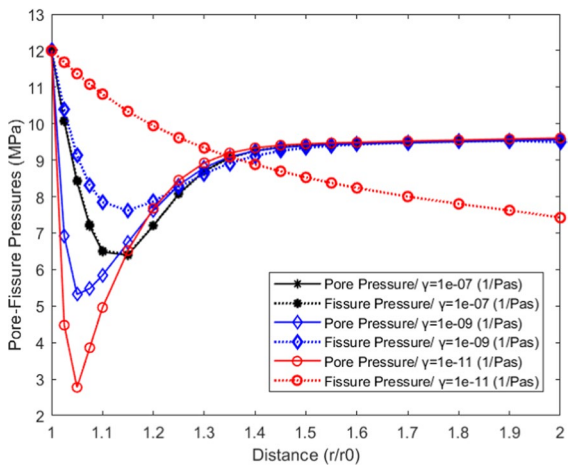

Fig. 22 Leakage term influence on pore-fissure pressure ($T_i = 5$ °C

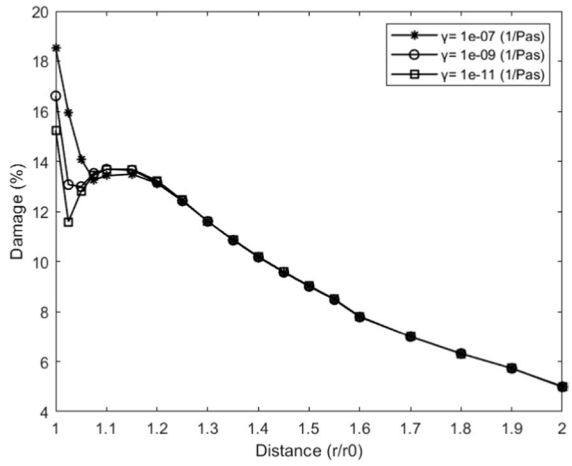

Fig. 23 Leakage term influence on damage ($T_i = 5$ °C

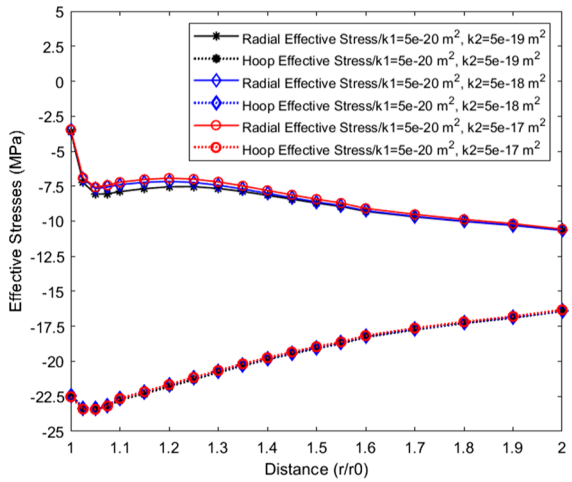

Fig. 24 Influence on the effective stress keeping the permeability of the porous domain constant and varying the permeability of the fissure network ($T_i = 5$ °C)

two phases. It can be outlined that rocks with low capability of mass transfer between the phases are vulnerable to potential fracturing due to stress relief and extreme pore pressure drop.

As far as it concerns the damage, the lower the leakage term is, the less damage appears in the vicinity of the wellbore at a specific timestep of injection, as seen in Fig. 23. Once the mass transfer is achieved and the two domains are in equilibrium the damage will increase and the rock can then be considered as a single-phase medium.

4.4 Permeability influence on the results

Changing the permeability of the rock can influence the dissipation speed of the fluid inside the domain. For the estimation of the permeability influence to the effective stresses and pore-fissure pressures, the permeability of the porous domain kept constant, while the permeability of the fissure network varied. The internal wellbore temperature of 5 °C is used

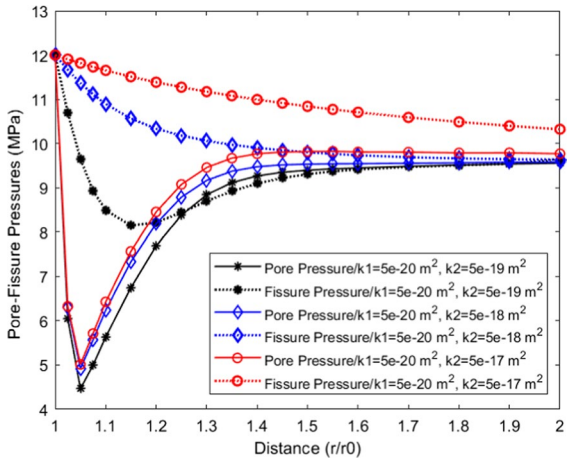

Fig. 25 Influence on the pore-fissure pressure keeping the permeability of the porous domain constant and varying the permeability of the fracture network ($T_i = 5$ °C)

indicating the scenario of injecting CO_2 at -5 °C. Figure 24 presents the permeability influence on the effective stresses, while Fig. 25 the permeability influence on the pore and fissure pressures.

It can be seen in Fig. 24 that the effective stresses are not influenced significantly by the permeability. However, changing the permeability, the difference between the pore and fissure network pressure can increase. Consequently, more time will be needed for them to achieve equilibrium (see Fig. 25).

5 Conclusions

The developed theoretical THM model, integrating elastoplastic material behaviour and damage evolution in double porosity fractured media, represents a significant advancement in the understanding and simulation capabilities of geomechanical systems. The model offers a comprehensive exploration of deformability, fluid flow, and heat transfer phenomena. By ensuring equilibrium, adhering to constitutive laws, and satisfying boundary conditions through meticulous global and local solution schemes, the model provides a robust framework for accurate simulations. Implemented using the Finite Element Method (FEM) in MATLAB, the numerical model demonstrates its capability to reproduce results from prior studies and experimental triaxial tests. This validation underscores the reliability of the model in capturing critical geomechanical phenomena.

Furthermore, the model's sensitivity to material strength, leakage term, and permeability highlights its potential for in-depth analyses. A suggested sensitivity analysis of mechanical critical state mechanics parameters offers a pathway to enhance the model's versatility and applicability under diverse loading conditions. Looking forward, the model holds promise for future investigations into multiphase flow and heat transfer between porosities (pores and fractures). This extension would enable a more detailed and accurate simulation of double porous media behaviour under realistic conditions.

The model's capacity to incorporate these additional complexities positions it as a valuable asset for researchers and practitioners seeking a comprehensive understanding of geomechanical systems. Overall, the theoretical THM model stands as a powerful and adaptable tool with broad applications in the field of geomechanics and porous media studies.

Acknowledgements This work was financially supported by the Engineering and Physical Sciences Research Council (EPSRC), with project Reference Number: EP/R51309X/1.

Author contributions NR did the methodology, investigation, numerical analysis and writing of the original draft. YG, BW and CTD contribute to the investigation, review, and editing. JM contribute to the methodology and reviewing. All authors contributed to the study conception and design. Constitutive and FEM model was created by Dr. NR. Validation of the model was performed by Dr. NR, Dr. YG, Dr. BW and Dr. CD, contributed to the presentation of the results. The first draft of the manuscript was written by Dr. NR and all authors commented on previous versions of the final manuscript. All authors read and approved the final manuscript.

Funding Open Access funding enabled and organized by CAUL and its Member Institutions

Data availability All participants state that the contents of the article do not contain unknown, fake or false data. The data generated in the present study are available from the corresponding author upon reasonable request.

Declarations

Conflict of interest All authors certify that they have no affiliations with or involvement in any organization or entity with

any financial interest or non-financial interest in the subject matter or materials discussed in this manuscript.

Ethics approval Not applicable.

Consent to publish The Authors confirm: that neither the manuscript nor any parts of its content are currently under consideration or published in another journal; that its publication has been approved by all co-authors; all of the material is owned by the authors and/or no permissions are required.

Appendices

Appensix 1. Bounding surface plasticity model details

The equation describing the bounding surface for different types of rocks was adopted based on Khalili et al. (2005), Reppas et al. (2020) and Reppas et al. (2022) as follows:

$$f\left(\breve{p}',\breve{q},\breve{p}_c'\right)=\frac{\breve{q}}{M_{cs}\breve{p}'}-\left(\frac{ln\left(\breve{p}_c'/\breve{p}'\right)}{lnR}\right)^{1/m}=0 \quad (60)$$

where $\breve{p}'$ represents the current effective stress on the yield surface, $\breve{p}_c'$ controls the size of the bounding surface and is a function of the damage variable D and the plastic volumetric strain ε_v^p; and m is a calibrating parameter that controls the shape of the bounding surface and according to Yu (1998). For the value of $m=1$, the yield function is reduced to the original Cam-Clay model; R is a material constant that represents the ratio between $\breve{p}_c'$ and the value of $\breve{p}'$ at the crossing point of the yield function f with the critical state line in the $q-p'$. domain. For sandstone, according to Ma (2014), m can take values from 1.7 to 2.5 and R from 2 to 2.45. The adopted flow plasticity model can be found and validated in the research of Ma (2014) and Reppas et al. (2022).

For porous rock, if damage takes place, the dilatancy-induced plastic strain can be accommodated by the plastic potential of Khalili et al. (2005) as follows:

$$g\left(p',q,p_0\right)=q+\left(1+k_d\xi\right)M_{cs}p'ln\frac{p'}{p_o'} \quad (61)$$

where p_o' is a dummy variable controlling the size of the plastic potential according to Ma (2014).

The unit normal vector $\boldsymbol{n}$ at the at the stress state $\boldsymbol{\sigma'}$, as seen in Fig. 26, defines the direction of loading and can be determined by the general equations of Khalili et al. (2005) as follows:

$$\boldsymbol{n}=\pm\frac{\partial L/\partial\boldsymbol{\sigma'}}{\partial L/\partial\boldsymbol{\sigma'}}=\pm\frac{\partial f/\partial\boldsymbol{\sigma'}}{\partial f/\partial\boldsymbol{\sigma'}} \quad (62)$$

The components of $\boldsymbol{n}=\left[n_p\ n_q\right]^T$ at $\boldsymbol{\sigma'}$ can be expressed as:

$$n_p=\pm\frac{-\breve{p}/\left(\breve{p}'\left[1-1/\left(Mln\left(\breve{p}_c'/\breve{p}'\right)\right)\right]\right)}{\sqrt{\left\{-\breve{p}/\left(\breve{p}'\left[1-1/\left(Mln\left(\breve{p}_c'/\breve{p}'\right)\right)\right]\right)\right\}^2+1}} \quad (63)$$

$$n_q=\pm\frac{1}{\sqrt{\left\{-\breve{p}/\left(\breve{p}'\left[1-1/\left(Mln\left(\breve{p}_c'/\breve{p}'\right)\right)\right]\right)\right\}^2+1}} \quad (64)$$

Appensix 2. Hardening effects

The hardening modulus h_p is separated in two components, the plastic modulus h_b at stress point $\boldsymbol{\sigma'}$ and the arbitrary modulus h_f (the distance between the $\boldsymbol{\sigma'}$ and $\breve{\boldsymbol{\sigma}}'$), as:

$$h_p=h_b+h_f \quad (65)$$

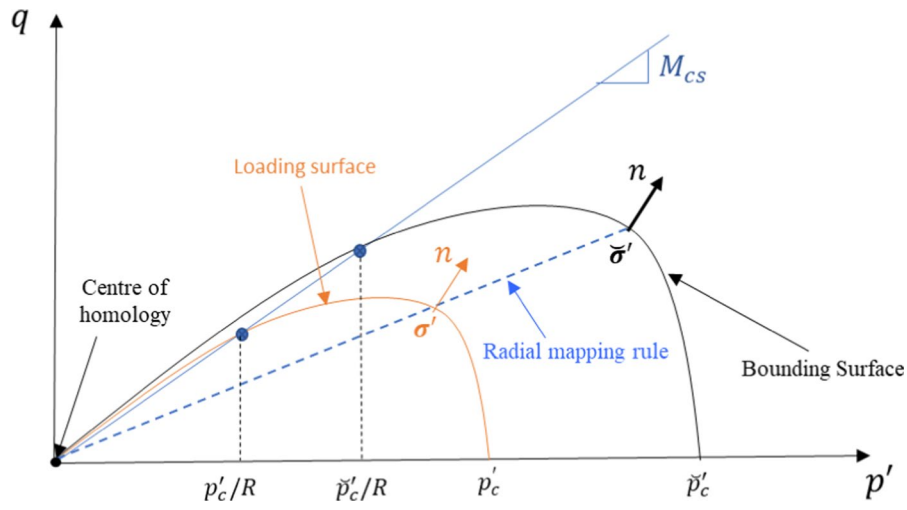

Fig. 26 Bounding surface, loading surface and mapping rule for compression of rock

Applying the plastic consistency condition at the bounding surface according to Khalili et al. (2008) and assuming that isotropic hardening of the bounding surface is connected with isotropic damage and plastic compressive volumetric strain, h_b can be expressed as:

$$h_b = -\frac{\partial f}{\partial \breve{p}_c'}\left(\frac{\partial \breve{p}_c'}{\partial \varepsilon_p^p} + \frac{\partial \breve{p}_c'}{\partial D}\frac{\dot{D}}{\dot{\varepsilon}_p^p}\right)\frac{x_p}{\partial f/\partial \breve{\sigma}'} \tag{66}$$

The arbitrary modulus h_f can be expressed based on the formulation proposed by Khalili et al. (2008) for sand and soil materials as:

$$h_f = \pm\left(\frac{\partial \breve{p}_c'}{\partial \varepsilon_p^p} + \frac{\partial \breve{p}_c'}{\partial D}\frac{\dot{D}}{\dot{\varepsilon}_p^p}\right)\frac{p'}{\breve{p}_c'}\left(\frac{\breve{p}_c'}{p_c'} - 1\right)m_p\left(\eta_p - \eta\right) \tag{67}$$

where $\breve{p}_c'$ and p_c' control the size of the bounding surface and the loading surface, respectively, m_p being a material parameter and $\eta = \frac{q}{p'}$ and $\eta_p = \left(1 - k_d\xi\right)M_{cs}$, with k being a material parameter. According to Khalili et al. (2005) h_f is zero at the bounding surface and infinite at the stress reversal point.

Appensix 3. FEM model shape functions and matrices

Finite Element modelling (FEM) was used to link the primary unknowns of those four governing equations to the applied boundary conditions. The primary unknowns are the displacement vector $\boldsymbol{u_d}$, the porous water pressure $\boldsymbol{p}_1$, the fissure saline water pressure $\boldsymbol{p}_2$ and the temperature of the solid medium $\boldsymbol{T}_s$. The general solutions of these differential equations are achieved by numerical approaches which give approximate results.

Appensix 3.1 Weak form

The weak form of the governing equations is obtained using the standard Galerkin weighted residual approach and application of the divergence operator as follows:

$$\int [N]^T\left(\nabla'^T\left(\left[\boldsymbol{S_{DTp}}\right]\left\{\nabla\left(\dot{\tilde{\boldsymbol{u}}}_{\boldsymbol{d}}\right)\right\}\right) + \beta_1\dot{\tilde{p}}_1\nabla'^T\{\boldsymbol{\delta}\} + \beta_2\dot{\tilde{p}}_2\nabla'^T\{\boldsymbol{\delta}\} - \frac{C_{Ts}}{C_f}\dot{\tilde{T}}_s\nabla'^T\{\boldsymbol{\delta}\} + \left\{\dot{\boldsymbol{F}}\right\}\right)d\Theta = 0 \tag{68}$$

$$\int [\boldsymbol{N}]^T\left(\nabla^T\left[\frac{\boldsymbol{k}_1}{\mu_f}\left(\nabla\tilde{p}_1 + \rho_f\{\boldsymbol{g}\}\right) + \varphi_1\Theta_1\nabla\tilde{T}_1\right] - \beta_1\{\boldsymbol{\delta}\}^T\nabla'\left\{\dot{\tilde{\boldsymbol{u}}}\right\} - \beta_{11}\dot{\tilde{p}}_1 + \beta_{12}\dot{\tilde{p}}_2 + \left(\beta_1 - \varphi_1\right)C_s\dot{\tilde{T}}_s + \Xi_1\right)d\Theta = 0 \tag{69}$$

$$\int [N]^T \left(\nabla^T \left[\frac{k_2}{\mu_f} \left(\nabla \tilde{p}_2 + \rho_f \{g\} \right) + \varphi_2 \Theta_2 \nabla \tilde{T}_2 \right] - \beta_2 \{\delta\}^T \nabla' \{\dot{\tilde{u}}\} - \beta_{22} \dot{\tilde{p}}_2 + \beta_{21} \dot{\tilde{p}}_1 + \left(\beta_2 - \varphi_2 \right) C_s \dot{\tilde{T}}_s + \Xi_2 \right) d\Theta = 0 \tag{70}$$

$$\int [N]^T \left(\nabla'^T \left[\varphi_s k_s \nabla T_s \right] \right) d\Theta = \int [N]^T \left(T_s \frac{C_s}{C_{fr}} \nabla' \{\dot{\tilde{u}}\} - T_s \left(\beta_1 - \varphi_1 \right) C_s \dot{\tilde{p}}_1 - T_s \left(\beta_2 - \varphi_2 \right) C_s \dot{\tilde{p}}_2 + \rho^s C_{ps} \dot{\tilde{T}}_s \right) d\Theta \tag{71}$$

where $\tilde{\boldsymbol{u}}_{\boldsymbol{d}}$, $\tilde{p}_1$ and $\tilde{p}_2$ are the approximate solutions of the differential Equations (68–71), $[\boldsymbol{N}]$ is the shape function and Θ is the element domain. The body force vector is ignored in this study for the sake of simplicity. The approximate solutions are computed in terms of the nodal values of the primary variables via the element shape functions:

$$\tilde{\boldsymbol{u}}_{\boldsymbol{d}} \cong [\boldsymbol{N}] \{\boldsymbol{u}_{\boldsymbol{d}}\} \tag{72}$$

$$\tilde{p}_1 \cong [\boldsymbol{N}] \{\boldsymbol{p}_1\} \tag{73}$$

$$\tilde{p}_2 \cong [\boldsymbol{N}] \{\boldsymbol{p}_2\} \tag{74}$$

$$\tilde{T}_s \cong [\boldsymbol{N}] \{\boldsymbol{T}_s\} \tag{75}$$

$$\{\boldsymbol{u}_{\boldsymbol{d}}\} = \{\boldsymbol{u}\} - 2\dot{D} \{\boldsymbol{u}^{\boldsymbol{e}}\} / (1 - D) \tag{76}$$

where $\{\boldsymbol{u}\}$, $\{\boldsymbol{p}_1\}$,$\{\boldsymbol{p}_2\}$, $\{\boldsymbol{T}_s\}$ are the vectors of the nodal values of the solid matrix displacement, pore saline water and fissure saline water pressure and temperature of the solid, respectively. $\{\boldsymbol{u}^{\boldsymbol{e}}\}$ is the vector of the nodal values of the solid matrix elastic displacement. This research uses two-dimensional four-node iso-parametric elements to represent the fractured porous medium. The associated shape functions can be found in the research of Gelet et al. (2012), and equal-order interpolation for all unknowns is selected for computational speed.

The finite element matrices in equations are listed below:

$$[\mathbf{K}] = \int \left[\nabla' \boldsymbol{N} \right]^T \left[\boldsymbol{S}^{\boldsymbol{ep}}(D, T) \right] \left[\nabla' \boldsymbol{N} \right] d\Theta \tag{77}$$

$$[\mathbf{C}]_{\boldsymbol{p}} = [\mathbf{C}]_{\boldsymbol{uT}} = \int \left[\nabla' \boldsymbol{N} \right]^T \{\boldsymbol{\delta}\} [\boldsymbol{N}] d\Theta \tag{78}$$

$$[\mathbf{C}]_{\boldsymbol{pT}} = [\mathbf{C}]_{\boldsymbol{Tu}} = \int [\boldsymbol{N}]^T \{\boldsymbol{\delta}\}^T \left[\nabla' \boldsymbol{N} \right] d\Theta \tag{79}$$

where the shape functions are as follows:

$$\mathrm{N} = \left[N^A N^B N^C N^D \right] \tag{80}$$

$\left[\nabla' \boldsymbol{N} \right]$ is the strain displacement matrix. For axisymmetric case, it can be expressed as follows:

$$\left[\nabla' \boldsymbol{N} \right] = \begin{bmatrix} \frac{\partial N^A}{\partial r} & 0 & \frac{\partial N^B}{\partial r} & 0 & \frac{\partial N^C}{\partial r} & 0 & \frac{\partial N^D}{\partial r} & 0 \\ 0 & \frac{\partial N^A}{\partial z} & 0 & \frac{\partial N^B}{\partial z} & 0 & \frac{\partial N^C}{\partial z} & 0 & \frac{\partial N^D}{\partial z} \\ \frac{N^A}{r} & 0 & \frac{N^B}{r} & 0 & \frac{N^C}{r} & 0 & \frac{N^D}{r} & 0 \\ \frac{\partial N^A}{\partial z} & \frac{\partial N^A}{\partial r} & \frac{\partial N^B}{\partial z} & \frac{\partial N^B}{\partial r} & \frac{\partial N^C}{\partial z} & \frac{\partial N^C}{\partial r} & \frac{\partial N^D}{\partial z} & \frac{\partial N^D}{\partial r} \end{bmatrix} \tag{81}$$

The Galerkin method involves interpolating the variations $\dot{\boldsymbol{u}}_{\boldsymbol{d}}$, $\dot{\boldsymbol{p}}_1$, $\dot{\boldsymbol{p}}_2$ and $\dot{\boldsymbol{T}}_{\boldsymbol{s}}$ through the shape functions N. Taking into consideration those shape functions, employing Green's theorem and substituting Equations (77–81) into Equations (68–71) results in:

$$
\begin{aligned}
&-\int \left[\nabla' N\right]^T \left[S_{DTp}\right]\left[\nabla' N\right]\left\{\dot{u}_d\right\}d\Theta+\int [N]^T\left[S_{DTp}\right]\left[\nabla' N\right]\left\{\dot{u}_d\right\}d\Gamma\\
&+\int \beta_1\left[\nabla' N\right]^T\{\delta\}[N]\left\{\dot{p}_1\right\}d\Theta-\int \beta_1[N]^T\{\delta\}[N]\left\{\dot{p}_1\right\}d\Gamma\\
&+\int \beta_2\left[\nabla' N\right]^T\{\delta\}[N]\left\{\dot{p}_2\right\}d\Theta-\int \beta_2[N]^T\{\delta\}[N]\left\{\dot{p}_2\right\}d\Gamma\\
&+\int \frac{C_{Ts}}{C_f}\left[\nabla' N\right]^T\{\delta\}[N]\left\{\dot{T}_s\right\}d\Theta-\int \frac{C_{Ts}}{C_f}[N]^T\{\delta\}[N]\left\{\dot{T}_s\right\}d\Gamma\\
&+\int [N]^T\left\{\dot{F}\right\}d\Theta=0
\end{aligned}
\tag{82}
$$

$$
\begin{aligned}
&-\int \beta_1[N]^T\{\delta\}^T\left[\nabla' N\right]\{\dot{u}\}d\Theta-\int \beta_{11}[N]^T[N]\left\{\dot{p}_1\right\}d\Theta\\
&+\int \beta_{12}[N]^T[N]\left\{\dot{p}_2\right\}d\Theta+\int \left(\beta_1-\varphi_1\right)C_s[N]^T[N]\left\{\dot{T}_s\right\}d\Theta\\
&-\int [\nabla N]^T\frac{k_1}{\mu_f}[\nabla N]\left\{p_1\right\}d\Theta+\int [N]^T\frac{k_1}{\mu_f}[\nabla N]\left\{p_1\right\}d\Gamma\\
&-\int [N]^T[N]\gamma\left\{\dot{p}_1\right\}d\Theta+\int [N]^T[N]\gamma\left\{\dot{p}_2\right\}d\Theta=0
\end{aligned}
\tag{83}
$$

$$
\begin{aligned}
&-\int \beta_2[N]^T\{\delta\}^T\left[\nabla' N\right]\{\dot{u}\}d\Theta-\int \beta_{22}[N]^T[N]\left\{\dot{p}_2\right\}d\Theta\\
&+\int \beta_{21}[N]^T[N]\left\{\dot{p}_2\right\}d\Theta+\int \left(\beta_2-\varphi_2\right)C_s[N]^T[N]\left\{\dot{T}_s\right\}d\Theta\\
&-\int [\nabla N]^T\frac{k_2}{\mu_f}[\nabla N]\left\{p_2\right\}d\Theta+\int [N]^T\frac{k_2}{\mu_f}[\nabla N]\left\{p_2\right\}d\Gamma\\
&-\int [N]^T[N]\gamma\left\{\dot{p}_2\right\}d\Theta+\int [N]^T[N]\gamma\left\{\dot{p}_1\right\}d\Theta=0
\end{aligned}
\tag{84}
$$

$$
\begin{aligned}
&-\int [\nabla N]^T\varphi_s k_s[\nabla N]\left\{T_s\right\}d\Theta+\int [N]^T\varphi_s k_s[\nabla N]\left\{T_s\right\}d\Gamma\\
&-\int T_s\frac{C_s}{C_{fr}}[N]^T\{\delta\}^T\left[\nabla' N\right]\{\dot{u}\}d\Theta\\
&+\int T_s\left(\beta_1-\varphi_1\right)C_s[N]^T[N]\left\{\dot{p}_1\right\}d\Theta\\
&+\int T_s\left(\beta_2-\varphi_2\right)C_s[N]^T[N]\left\{\dot{p}_2\right\}d\Theta\\
&-\int \rho^s C_{ps}[N]^T[N]\left\{\dot{T}_s\right\}d\Theta=0
\end{aligned}
\tag{85}
$$

where Γ is the element domain.

Equations (82) to (85) are presented in a contracted FEM form as follows:

$$
\begin{aligned}
&[\mathbf{K}]\left\{\dot{u}_d\right\}-\beta_1[\mathbf{C}]_p\left\{\dot{p}_1\right\}-\beta_2[\mathbf{C}]_p\left\{\dot{p}_2\right\}\\
&-\frac{C_{Ts}}{C_f}[\mathbf{C}]_{uT}\left\{\dot{T}_s\right\}=\left\{\dot{W}_d\right\}
\end{aligned}
\tag{86}
$$

$$
\begin{aligned}
&-\beta_1[\mathbf{C}]_{pT}\{\dot{u}\}-\beta_{11}[\mathbf{M}]\left\{\dot{p}_1\right\}+\beta_{12}[\mathbf{M}]\left\{\dot{p}_2\right\}\\
&+\left(\beta_1-\varphi_1\right)C_s[\mathbf{M}]\left\{\dot{T}_s\right\}\\
&-[\mathbf{H}]_{1p}\left\{p_1\right\}-\gamma[\mathbf{M}]\left\{\dot{p}_1-\dot{p}_2\right\}=\left\{\dot{W}_1\right\}
\end{aligned}
\tag{87}
$$

$$
\begin{aligned}
&-\beta_2[\mathbf{C}]_{pT}\{\dot{u}\}-\beta_{22}[\mathbf{M}]\left\{\dot{p}_2\right\}+\beta_{21}[\mathbf{M}]\left\{\dot{p}_1\right\}+C_s[\mathbf{M}]\left\{\dot{T}_s\right\}\\
&-[\mathbf{H}]_{2p}\left\{p_2\right\}-\gamma[\mathbf{M}]\left\{\dot{p}_2-\dot{p}_1\right\}=\left\{\dot{W}_2\right\}
\end{aligned}
\tag{88}
$$

$$
\begin{aligned}
&-T_s\frac{C_s}{C_{fr}}[\mathbf{C}]_{Tu}\{\dot{u}\}+T_s(\beta_1-\varphi_1)C_s[\mathbf{M}]\left\{\dot{p}_1\right\}\\
&+T_s\left(\beta_2-\varphi_2\right)C_s[\mathbf{M}]\left\{\dot{p}_2\right\}\\
&-\rho^s C_{ps}[\mathbf{M}]\left\{\dot{T}_s\right\}-[\mathbf{H}]_{Ts}\left\{T_s\right\}=-\left\{\mathbf{R_s}\right\}
\end{aligned}
\tag{89}
$$

Appensix 3.2 Time integration

To determine the solution of the coupled problem in time, the rate form of the discretized equation needs to be integrated over time. Specifically, the integration of an arbitrary function y over the interval time Δt is taken as:

$$
\begin{aligned}
&\int_t^{t+\Delta t} y(t)dt=\left[(1-\beta)y_t+\beta y_{t+\Delta t}\right]\Delta t=\left(y_t+\beta\Delta y\right)\Delta t\\
&\Delta y=y_{t+\Delta t}-y_t
\end{aligned}
\tag{90}
$$

where y_t is the value of y at the time t, and β represents the type of approximation applied to the time integration. $\beta = 1$ is used for backward interpolation, $\beta = 0.5$ for central interpolation and $\beta = 0$ for forwarding interpolation.

Applying the spatially discretized function Eq. (90), the Eqs. (86–89) can be rearranged as follows:

$$[\mathbf{K}]\{\boldsymbol{u_d}\}^{t+\Delta t} - \beta_1[\mathbf{C}]_p\{\boldsymbol{p}_1\}^{t+\Delta t} - \beta_2[\mathbf{C}]_p\{\boldsymbol{p}_2\}^{t+\Delta t} - \frac{C_{Ts}}{C_f}[\mathbf{C}]_T\{\boldsymbol{T}_s\}^{t+\Delta t} = \{\boldsymbol{R_d}\}^{t+\Delta t} \tag{91}$$

$$\begin{aligned}
&- \beta_1[\mathbf{C}]_{\boldsymbol{pT}}\{\boldsymbol{u}\}^{t+\Delta t} - \beta_{11}[\mathbf{M}]\{\boldsymbol{p}_1\}^{t+\Delta t} + \beta_{12}[\mathbf{M}]\{\boldsymbol{p}_2\}^{t+\Delta t} + (\beta_1 - \varphi_1)C_s[\mathbf{M}]\{\boldsymbol{T}_s\}^{t+\Delta t} \\
&\quad - \beta\Delta t[\mathbf{H}]_{1p}\{\boldsymbol{p}_1\}^{t+\Delta t} + \beta\Delta t\gamma[\mathbf{M}]\left[\{\boldsymbol{p}_2\}^{t+\Delta t} - \{\boldsymbol{p}_1\}^{t+\Delta t}\right] \\
&\quad = -\beta_1[\mathbf{C}]_{\mathbf{pT}}\{\boldsymbol{u}\}^{t} - \beta_{11}[\mathbf{M}]\{\boldsymbol{p}_1\}^{t} + \beta_{12}[\mathbf{M}]\{\boldsymbol{p}_2\}^{t} + (\beta_1 - \varphi_1)C_s[\mathbf{M}]\{\boldsymbol{T}_s\}^{t} \\
&\quad + (1-\beta)\Delta t[\mathbf{H}]_{1p}\{\boldsymbol{p}_1\}^{t} - (1-\beta)\beta t\gamma[\mathbf{M}]\left[\{\boldsymbol{p}_2\}^{t+\Delta t} - \{\boldsymbol{p}_1\}^{t+\Delta}\right] \\
&\quad + \beta\Delta t\{\boldsymbol{W}_1\}^{t+\beta t} + (1-\beta)\Delta t\{\boldsymbol{W}_1\}^{t}
\end{aligned} \tag{92}$$

$$\begin{aligned}
&- \beta_2[\mathbf{C}]_{\boldsymbol{pT}}\{\boldsymbol{u}\}^{t+\Delta t} - \beta_{22}[\mathbf{M}]\{\boldsymbol{p}_2\}^{t+\Delta t} + \beta_{21}[\mathbf{M}]\{\boldsymbol{p}_1\}^{t+\Delta t} \\
&\quad + (\beta_2 - \varphi_2)C_s[\mathbf{M}]\{\boldsymbol{T}_s\}^{t+\Delta t} - \beta\Delta t[\mathbf{H}]_{2p}\{\boldsymbol{p}_2\}^{t+\Delta t} \\
&\quad + \beta\Delta t\gamma[\mathbf{M}]\left[\{\boldsymbol{p}_1\}^{t+\Delta t} - \{\boldsymbol{p}_2\}^{t+\Delta t}\right] \\
&\quad = -\beta_2[\mathbf{C}]_{\boldsymbol{pT}}\{\boldsymbol{u}\}^{t} - \beta_{22}[\mathbf{M}]\{\boldsymbol{p}_2\}^{t} + \beta_{21}[\mathbf{M}]\{\boldsymbol{p}_2\}^{t} \\
&\quad + (\beta_2 - \varphi_2)C_s[\mathbf{M}]\{\boldsymbol{T}_s\}^{t} + (1-\beta)\Delta t[\mathbf{H}]_{2p}\{\boldsymbol{p}_2\}^{t} \\
&\quad - (1-\beta)\Delta t\left[\{\boldsymbol{p}_1\}^{t+\Delta t} - \{\boldsymbol{p}_2\}^{t+\Delta t}\right] + \beta\Delta t\{\boldsymbol{W}_2\}^{t+\Delta t} \\
&\quad + (1-\beta)\Delta t\{\boldsymbol{W}_2\}^{t}
\end{aligned} \tag{93}$$

$$\begin{aligned}
&- T_s\frac{C_s}{C_{fr}}[\mathbf{C}]_{\mathbf{Tu}}\{\boldsymbol{u}\}^{t+\Delta t} + T_s(\beta_1 - \varphi_1)C_s[\mathbf{M}]\{\boldsymbol{p}_1\}^{t+\Delta t} \\
&\quad + T_s(\beta_2 - \varphi_2)C_s[\mathbf{M}]\{\boldsymbol{p}_2\}^{t+\Delta t} - \rho^s C_{ps}[\mathbf{M}]\{\boldsymbol{T}_s\}^{t+\Delta t} \\
&\quad - \beta\Delta t[\mathbf{H}]_{\mathrm{Ts}}\{\boldsymbol{T}_s\}^{t+\Delta t} \\
&\quad = -T_s\frac{C_s}{C_{fr}}[\mathbf{C}]_{\mathbf{Tu}}\{\boldsymbol{u}\}^{t} + T_s(\beta_1 - \varphi_1)C_s[\mathbf{M}]\{\boldsymbol{p}_1\}^{t} \\
&\quad + T_s(\beta_2 - \varphi_2)C_s[\mathbf{M}]\{\boldsymbol{p}_2\}^{t} - \rho^s C_{ps}[\mathbf{M}]\{\boldsymbol{T}_s\}^{t} \\
&\quad + (1-\beta)\Delta t[\mathbf{H}]_{\mathrm{Ts}}\{\boldsymbol{T}_s\}^{t} - \beta\Delta t\{\boldsymbol{R}_s\}^{t+\Delta t} - (1-\beta)\Delta t\{\boldsymbol{R}_s\}^{t}
\end{aligned} \tag{94}$$

Appensix 3.3 Modified Euler's forward scheme

The procedure followed to solve the ordinary differential equations in this work is the modified Euler's algorithm presented in the following steps:

1st step A time step $\Delta\breve{t}$ is used to calculate from any current effective stress $\sigma'_{\breve{t}}$ and current damage variable $D_{\breve{t}}$ the same variables at the next incremental step as follows:

$$\sigma'_{\breve{t}+\Delta\breve{t}} = \sigma'_{\breve{t}} + \Delta\sigma' \tag{95}$$

$$D_{\breve{t}+\Delta\breve{t}} = D_{\breve{t}} + \Delta D \tag{96}$$

where $\Delta\sigma'$ the increment of effective stress and ΔD is the cumulative damage.

2nd step According to Sloan et al. (2001) and Habte (2006) a pseudo time sub increment is introduced $\left(0 < \Delta\bar{t}_w < 1\right)$.

$\Delta\bar{t}_w$ is the size of the wth sub increment and Δt is the total time increment in which the incremental strain $\Delta\varepsilon$ is acting. Using now the explicit Euler's method at the end of the pseudo time step $\Delta\bar{t}_w$, the stress and the hardening and damage parameters can be determined as:

$$\sigma'_{w+1} = \sigma'_w + \frac{1}{2}\left(\Delta\sigma'_1 + \Delta\sigma'_2\right) \tag{97}$$

$$\breve{p}'_{c(w+1)} = \breve{p}'_{cw} + \frac{1}{2}\left(\Delta\breve{p}'_{c1} + \Delta\breve{p}'_{c2}\right) \tag{98}$$

$$D_{w+1} = D_w + \frac{1}{2}\left(\Delta D_1 + \Delta D_2\right) \tag{99}$$

where $\Delta\sigma'_1$, $\Delta\breve{p}'_{c1}$ are calculated by the explicit forward scheme at the stress state $\Delta\sigma'_w$ and plastic hardening parameter $\breve{p}'_{cw}$, respectively. ΔD_1 is computed at the stress state $\sigma'_w + \Delta\sigma'_1$ and damage condition D_w; $\Delta\sigma'_2$, $\Delta\breve{p}'_{c2}$ are calculated by the explicit forward scheme at the stress state $\sigma'_{w+1} + \Delta\sigma'_1$ and plastic hardening parameter $\breve{p}'_{cw+1} + \Delta\breve{p}'_{c1}$, respectively. ΔD_2 is computed at the stress state $\sigma'_w + \Delta\sigma'_1 + \Delta\sigma'_2$ and damage condition $D_w + \Delta D_1$

Then all these variables are updated. Afterwards, Euler's scheme is applied to compute another set of these variable using the updated values.

3rd step An error for the given step is then determined, which is the difference between the second-order Euler's modified approach and the first-order Euler's solution. If the error is too large, then the strain increment is subdivided into smaller steps using an expression for the primary error term as follows:

The local error for the calculated values of σ'_{w+1} and $\breve{p}'_{c(w+1)}$ is determined as the difference between the second order modified Euler and the first order Euler scheme.

The relative error of the modified Euler solution is obtained using the following form:

$$R_w = max\left(\frac{E_w\left(\sigma'_{w+1}\right)}{\sigma'_{w+1}}, \frac{\left|E_w\left(\breve{p}'_{c(w+1)}\right)\right|}{\breve{p}'_{c(w+1)}}, \frac{\left|E_w\left(D_{w+1}\right)\right|}{D_{w+1}}\right) \tag{100}$$

where

$$E_w\left(\sigma'_{w+1}\right) = \frac{1}{2}\left(\Delta\sigma'_2 + \Delta\sigma'_1\right) \tag{101}$$

$$E_w\left(\breve{p}'_{c(w+1)}\right) = \frac{1}{2}\left(\Delta\breve{p}'_{c2} + \Delta\breve{p}'_{c1}\right) \tag{102}$$

$$E_w\left(D_{w+1}\right) = \frac{1}{2}\left(\Delta D_2 + \Delta D_1\right) \tag{103}$$

Suppose the calculated local error is greater than the specified tolerance. In that case, the proposed solution is rejected, and the process is repeated using now a smaller sub-step size until a successful sub increment is achieved. Once the local error satisfies the limitation 2nd step is updated.

For the current study, the adopted prescribed error tolerance for the yield surface is set to 10^{-9}, the stress error tolerance between the first-order Euler method and the second-order modified Euler method is set to 10^{-6} and the damage error tolerance is set to 10^{-6} (Ma 2014).

4th step The integration scheme is fully achieved when the total imposed strain increment is applied.

The matrices for hydraulic conductivity and heat conduction are:

$$[\mathbf{H}]_{1p} = \int [\nabla \boldsymbol{N}]^T \frac{\boldsymbol{k}_1}{\mu_f} [\nabla \boldsymbol{N}] d\Theta \tag{104}$$

$$[\mathbf{H}]_{2p} = \int [\nabla \boldsymbol{N}]^T \frac{\boldsymbol{k}_2}{\mu_f} [\nabla \boldsymbol{N}] d\Theta \tag{105}$$

$$[\mathbf{H}]_{Ts} = \int [\nabla \boldsymbol{N}]^T \varphi_s k_s [\nabla \boldsymbol{N}] d\Theta \tag{106}$$

The mass matrix is:

$$[\mathbf{M}] = \int [\boldsymbol{N}]^T [\boldsymbol{N}] d\Theta \tag{107}$$

The matrices of the load vector corresponding to the nodal forces and fluxes are as follows:

$$\left\{\dot{\boldsymbol{W}}_d\right\} = \int [\boldsymbol{N}]^T \left\{\dot{\boldsymbol{F}}\right\} d\Theta + \int [\boldsymbol{N}]^T \left\{ \boldsymbol{Traction} \right\} d\Gamma \tag{108}$$

$$\left\{\dot{\boldsymbol{W}}_1\right\} = \int [\boldsymbol{N}]^T \left\{\mathbf{q}_1\right\} d\Gamma \tag{109}$$

$$\left\{\dot{\boldsymbol{W}}_2\right\} = \int [\boldsymbol{N}]^T \left\{\mathbf{q}_2\right\} d\Gamma \tag{110}$$

$$\{\mathbf{R_s}\} = \int [N]^T \{r_s\} d\Gamma \tag{111}$$

where $\left\{ \dot{\boldsymbol{Traction}} \right\}$, $\{q_1\}$, $\{q_2\}$ and $\{r_s\}$ vectors of the nodal traction force, pore and fissure water pressure influx and heat flux respectively and are defined as follows:

$$\left\{ \dot{\boldsymbol{Traction}} \right\} = [\boldsymbol{Sep}(D)] [\nabla' N] \{\dot{u}_d\} - \beta_1 \{\delta\} [N] \{\dot{p}_1\} - \beta_2 \{\delta\} [N] \{\dot{p}_2\} - \frac{C_{Ts}}{C_f} \{\delta\} [N] \{\dot{T}_s\} \tag{112}$$

$$\{\mathbf{q}_1\} = -\frac{k_1}{\mu_f} [\nabla N] \{p_1\} \tag{113}$$

$$\{\mathbf{q}_2\} = -\frac{k_2}{\mu_f} [\nabla N] \{p_2\} \tag{114}$$

$$\{r_s\} = \varphi_s k_s [\nabla N] \{T_s\} \tag{115}$$

References

Aifantis E (1980) On the problem of diffusion in solids. Acta Mech 37:265–296

Aifantis EC, Beskos D (1980) Heat extraction from hot dry rocks. Mech Res Commun 7:165–170

Aliyu MD, Finkbeiner T, Chen H-P, Archer RA (2023) A three-dimensional investigation of the thermoelastic effect in an enhanced geothermal system reservoir. Energy 262:125466

Alonso J, Navarro V, Calvo B, Asensio L (2012) Hydro-mechanical analysis of CO_2 storage in porous rocks using a critical state model. Int J Rock Mech Min Sci 54:19–26

Bai Y (2016) Coupled thermo-hydro-mechanical (THM) model for multiphase flow through deformable porous media with double porosity. Doctor of Philosophy, The University of New South Wales

Bai T, Tahmasebi P (2022) Coupled hydro-mechanical analysis of seasonal underground hydrogen storage in a saline aquifer. J Energy Storage 50:104308

Biot MA (1941) General theory of three-dimensional consolidation. J Appl Phys 12:155–164

Bowen RM (1982) Compressible porous media models by use of the theory of mixtures. Int J Eng Sci 20:697–735

Bowen R, Garcia D (1970) On the thermodynamics of mixtures with several temperatures. Int J Eng Sci 8:63–83

Brünig M, Michalski A (2017) A stress-state-dependent continuum damage model for concrete based on irreversible thermodynamics. Int J Plast 90:31–43

Busetti S, Mish K, Reches ZE (2012) Damage and plastic deformation of reservoir rocks: Part 1. Damage fracturing. AAPG Bull 96:1687–1709

Cheng A-D, Abousleiman Y, Roegiers J-C (1993) Review of some poroelastic effects in rock mechanics. Int J Rock Mech Min Sci Geomech Abstr 30:1119–1126

Cuss R, Rutter E, Holloway R (2003) The application of critical state soil mechanics to the mechanical behaviour of porous sandstones. Int J Rock Mech Min Sci 40:847–862

Damirchi BV, Bitencourt LA Jr, Manzoli OL, Dias-Da-Costa D (2022) Coupled hydro-mechanical modelling of saturated fractured porous media with unified embedded finite element discretisations. Comput Methods Appl Mech Eng 393:114804

De La Cruz V, Spanos T (1989) Thermomechanical coupling during seismic wave propagation in a porous medium. J Geophys Res Solid Earth 94:637–642

Detournay E, Cheng A-D (1988) Poroelastic response of a borehole in a non-hydrostatic stress field. Int J Rock Mech Min Sci Geomech Abstr 25:171–182

Gelet R, Loret B, Khalili N (2012) Borehole stability analysis in a thermoporoelastic dual-porosity medium. Int J Rock Mech Min Sci 50:65–76

Gerogiannopoulos NG, Brown ET (1978) The critical state concept applied to rock. Int J Rock Mech Min Sci Geomech Abstr 15:1–10

Goodman M, Cowin S (1972) A continuum theory for granular materials. Arch Ration Mech Anal 44:249–266

Habte MA (2006) Numerical and constitutive modelling of monotonic and cyclic loading in variably saturated soils. University of New South Wales, Sydney

Huang S, Liu Q, Liu Y, Ye Z, Cheng A (2018) Freezing strain model for estimating the unfrozen water content of saturated rock under low temperature. Int J Geomech 18:04017137

Jing L, Hudson J (2002) Numerical methods in rock mechanics. Int J Rock Mech Min Sci 39:409–427

Johnson E, Cleary MP (1991) Implications of recent laboratory experimental results for hydraulic fractures. In: Low permeability reservoirs symposium. OnePetro

Kachanov L (1980) Crack and damage growth in creep—a combined approach. Int J Fract 16:R179–R181

Kazemi H (1969) Pressure transient analysis of naturally fractured reservoirs with uniform fracture distribution. Soc Pet Eng J 9:451–462

Khaledi K, Hamdi P, Winhausen L, Jalali M, Jaeggi D, Amann F (2021) Unloading induced absolute negative pore pressures in a low permeable clay shale. Eng Geol 295:106451

Khalili N (2008) Two-phase fluid flow through fractured porous media with deformable matrix. Water Resour Res. https://doi.org/10.1029/2007WR006555

Khalili N, Loret B (2001) An elasto-plastic model for non-isothermal analysis of flow and deformation in unsaturated porous media: formulation. Int J Solids Struct 38:8305–8330

Khalili N, Selvadurai A (2003) A fully coupled constitutive model for thermo-hydro-mechanical analysis in elastic media with double porosity. Geophys Res Lett 30:1–5

Khalili N, Valliappan S (1996) Unified theory of flow and deformation in double porous media. Eur J Mech A Solids 15:321–336

Khalili N, Habte M, Valliappan S (2005) A bounding surface plasticity model for cyclic loading of granular soils. Int J Numer Methods Eng 63:1939–1960

Khalili N, Habte MA, Zargarbashi S (2008) A fully coupled flow deformation model for cyclic analysis of unsaturated soils including hydraulic and mechanical hystereses. Comput Geotech 35:872–889

Khalili N, Uchaipichat A, Javadi AA (2010) Skeletal thermal expansion coefficient and thermo-hydro-mechanical constitutive relations for saturated homogeneous porous media. Mech Mater 42:593–598

Kolditz O, Shao H, Wang W, Bauer S (2016) Thermo-hydro-mechanical chemical processes in fractured porous media: modelling and benchmarking. Springer, Berlin

Kong L, Xie H, Li C (2023) Coupled microplane and micromechanics model for describing the damage and plasticity evolution of quasi-brittle material. Int J Plast 162:103549

Lemaitre J (1985) A continuous damage mechanics model for ductile fracture. J Eng Mater Technol 107:83–89

Liu Z, Yu X (2011) Coupled thermo-hydro-mechanical model for porous materials under frost action: theory and implementation. Acta Geotech 6:51–65

Ma J (2014) Coupled flow deformation analysis of fractured porous media subject to elasto-plastic damage. PhD thesis, The University of New South Wales, Australia

Ma J (2016) An elastoplastic model for partially saturated collapsible rocks. Rock Mech Rock Eng 49:455–465

Ma J, Wang J (2016) A stress-induced permeability evolution model for fissured porous media. Rock Mech Rock Eng 49:477–485

Ma J, Zhao G-F (2018) Borehole stability analysis in fractured porous media associated with elastoplastic damage response. Int J Geomech 18:04018022

Ma J, Zhao G, Khalili N (2016) A fully coupled flow deformation model for elasto-plastic damage analysis in saturated fractured porous media. Int J Plast 76:29–50

Ma J, Chen J, Chen W, Huang L (2022) A coupled thermal-elastic-plastic-damage model for concrete subjected to dynamic loading. Int J Plast 153:103279

Maedo MA, Sánchez M, Fabbri H, Cleto P, Guimarães LJ, Manzoli OL (2021) Coupled thermo-hydro-mechanical numerical modeling of evolving fractures in rocks. Rock Mech Rock Eng 54:3569–3591

Mahmoodpour S, Singh M, Bär K, Sass I (2022) Thermo-hydro-mechanical modeling of an enhanced geothermal system in a fractured reservoir using carbon dioxide as heat transmission fluid—a sensitivity investigation. Energy 254:124266

Masters I, Pao WK, Lewis R (2000) Coupling temperature to a double-porosity model of deformable porous media. Int J Numer Methods Eng 49:421–438

Mctigue DF (1986) Thermoelastic response of fluid-saturated porous rock. J Geophys Res Solid Earth 91:9533–9542

Mortara G (2009) A hierarchical single yield surface for frictional materials. Comput Geotech 36:960–967

Navarro V, Alonso J, Calvo B, Sánchez J (2010) A constitutive model for porous rock including effects of bond strength degradation and partial saturation. Int J Rock Mech Min Sci 47:1330–1338

Neaupane KM, Yamabe T, Yoshinaka R (1999) Simulation of a fully coupled thermo–hydro–mechanical system in freezing and thawing rock. Int J Rock Mech Min Sci 36(5):563–580

Nishimura S, Gens A, Olivella S, Jardine RJ (2009) THM-coupled finite element analysis of frozen soil: formulation and application. Géotechnique 59(3):159–171

Paluszny A, Thomas RN, Saceanu MC, Zimmerman RW (2020) Hydro-mechanical interaction effects and channelling in three-dimensional fracture networks undergoing growth and nucleation. J Rock Mech Geotech Eng 12:707–719

Reppas N, Gui Y, Wetenhall B, Davie C, Ma J (2020) Elasto-plastic behavior of rock during temperature drop. Int J Geotech Geol Eng 14:177–184

Reppas N, Davie C, Wetenhall B, Gui YL, Ma J (2022) Numerical simulation of triaxial experimental results on sandstone using critical state mechanics. In; 56th U.S. rock mechanics/geomechanics symposium. ARMA-2022–2184

Reppas N, Davie CT, Gui Y, Wetenhall B, Graham SP (2023) The effects of cooling on fine-grained sandstone in relation to wellbore injection of carbon dioxide. Rock Mech Rock Eng 56:1–19

Rice JR, Cleary MP (1976) Some basic stress diffusion solutions for fluid-saturated elastic porous media with compressible constituents. Rev Geophys 14:227–241

Saeedmonir S, Khoei AR (2022) Multiscale modeling of coupled thermo-hydro-mechanical analysis of heterogeneous porous media. Comput Methods Appl Mech Eng 391:114518

Schultz R, Siddharthan R (2005) A general framework for the occurrence and faulting of deformation bands in porous granular rocks. Tectonophysics 411:1–18

Shah KR (1997) An elasto-plastic constitutive model for brittle-ductile transition in porous rocks. Int J Rock Mech Min Sci 34:283

Sheldon HA, Barnicoat AC, Ord A (2006) Numerical modelling of faulting and fluid flow in porous rocks: an approach based on critical state soil mechanics. J Struct Geol 28:1468–1482

Shen F, Kang G, Lam YC, Liu Y, Zhou K (2019) Thermo-elastic-viscoplastic-damage model for self-heating and mechanical behavior of thermoplastic polymers. Int J Plast 121:227–243

Shojaei A, Taleghani AD, Li G (2014) A continuum damage failure model for hydraulic fracturing of porous rocks. Int J Plast 59:199–212

Sloan SW, Abbo AJ, Sheng D (2001) Refined explicit integration of elastoplastic models with automatic error control. Eng Comput 18:121–194

Spiezia N, Salomoni VA, Majorana CE (2016) Plasticity and strain localization around a horizontal wellbore drilled through a porous rock formation. Int J Plast 78:114–144

Tan X, Chen W, Tian H, Cao J (2011) Water flow and heat transport including ice/water phase change in porous media: numerical simulation and application. Cold Reg Sci Technol 68:74–84

Vilarrasa V, Laloui L (2016) Impacts of thermally induced stresses on fracture stability during geological storage of CO_2. Energy Procedia 86:411–419

Vilarrasa V, Silva O, Carrera J, Olivella S (2013) Liquid CO_2 injection for geological storage in deep saline aquifers. Int J Greenh Gas Control 14:84–96

Von Terzaghi K (1923) Die Berechnug der durchlassigkeit des tones aus dem verlauf der hydromechanischen spannungserscheinungen. Sitzungsber Akad Wiss (wien) Math Naturwiss Kl Abt Iia 132:125–138

Voyiadjis GZ, Kattan PI (2005) Damage mechanics. CRC Press, Boca Raton

Warren J, Root PJ (1963) The behavior of naturally fractured reservoirs. Soc Pet Eng J 3:245–255

Wong TF, David C, Zhu W (1997) The transition from brittle faulting to cataclastic flow in porous sandstones: mechanical deformation. J Geophys Res Solid Earth 102:3009–3025

Yazdchi M, Valliappan S, Zhang W (1996) A continuum model for dynamic damage evolution of anisotropic brittle materials. Int J Numer Methods Eng 39:1555–1583

Yu HS (1998) CASM: a unified state parameter model for clay and sand. Int J Numer Anal Methods Geomech 22:621–653

Zhang J, Liu W, Zhu Q, Shao J (2023) A novel elastic–plastic damage model for rock materials considering microstructural degradation due to cyclic fatigue. Int J Plast 160:103496

Zhao L-Y, Zhu Q-Z, Shao J-F (2018) A micro-mechanics based plastic damage model for quasi-brittle materials under a large range of compressive stress. Int J Plast 100:156–176